Elastic Light Scattering of Silicon and Diamond Microspheres Excited by Femtosecond Laser Written Glass and Diamond Waveguides

by

Nurperi Yavuz

A Dissertation Submitted to the

Graduate School of Sciences and Engineering

in Partial Fulfillment of the Requirements for the Degree of

Master of Science

in

Optoelectronics and Photonics Engineering

KOÇ
UNIVERSITY

December 18, 2018

MSc Thesis

Koç University

Koç University Graduate School of Sciences and Engineering

This is to certify that, I have examined this copy of a master's thesis by

Nurperi Yavuz

and have found that, it is complete and satisfactory in all respects, and that any and all revisions required by the final examining committee have been made.

Committee Members:

_____

Prof. Ali SERPENGÜZEL

_____

Prof. Mehmet Burçin ÜNLÜ

_____

Assoc. Prof. Kaan GÜVEN

Date: _____

ABSTRACT

Elastic light scattering of silicon and diamond microspheres excited by femtosecond (fs)-laser written glass and diamond waveguides is studied in order to assemble an all diamond optical system towards integrated diamond photonics applications.

Transverse electrically (TE) and transverse magnetically (TM) polarized light from a wavelength tunable laser operating in the near-infrared region is coupled to a 1 mm silicon sphere by using the Gorilla and Eagle$^{2000™}$ glass optical waveguides. Silicon sphere elastic scattering characteristics are gathered on both glass and diamond optical waveguides, in order to examine diamond optical waveguide characteristics. After which, an all-diamond optical system is established with diamond sphere on fs-laser written diamond shallow waveguide.

The assembled diamond system integrates a Type-Ib (nitrogen impurity > 5 ppm) diamond microsphere with a fs-laser written Type-IIa (nitrogen impurity of 100 ppb) diamond waveguide. The diamond waveguide is fabricated by exploiting type II fabrication method to achieve stress induced waveguiding. TE and TM polarized light from a wavelength tunable laser operating in the near-infrared region is coupled to a 1 mm diamond sphere by using the diamond optical waveguide.

By carefully engineering the microsphere's high quality factor resonances, and further exploiting the nonlinear properties of existing nitrogen-vacancy (NV) centers in diamond microspheres and/or diamond waveguides in such configurations, it is possible to realize various applications in integrated diamond photonics.

ÖZET

Gelecekte tümleşik elmas fotonik uygulamalarında kullanılmak üzere, tüm bileşenleri elmas fotonik tabanında birleştirmek için, femtosaniye (fs)-lazer ile yazılmış sığ optik cam ve elmas dalgakılavuzlarına bağlaştırılmış silisyum ve elmas mikroyuvarların fısıldayan geçit kiplerinin esnek saçılmaları üzerinde çalışılmıştır.

Dalgaboyu değiştirilebilen yakın kızılaltı sürekli lazerden gelen enine elektrik (TE) ve enine manyetik (TM) kutuplu ışık ile 1 mm çapında silisyum yuvar arasındaki bağlaşma Gorilla ve Eagle$^{2000™}$ camlarına yazılmış sığ dalgakılavuzları ile yapılmıştır. Öncelikle silisyum mikroyuvarın elastik saçılma özellikleri cam ve elmas dalgakılavuzları ile gözlenmiştir. Daha sonra, bu verileri karşılaştırarak elmas sığ optik dalgakılavuzunun davranışı incelenmiş ve bu bilgiler tüm bileşenleri elmas olan düzeneğin incelenmesinde öncü olmuştur.

Tüm bileşenleri elmas olan düzenekte, bir Tür-1b (azot > milyonda 5 parça) elmas mikroçınlaç, ve bir fs-saniye lazer ile yazılmış Tür-2a (azot milyarda 100 parça) elmas sığ dalgakılavuzu kullanılmıştır. Sığ elmas dalgakılavuzu Tür 2 gerilme etkili lazer yazma yöntemiyle işlenmiştir. TE ve TM kutuplu dalgaboyu değiştirilebilen yakın kızılaltı sürekli uyarma lazeri elmas optik dalgakılavuzundan 1 mm elmas mikroyuvara bağlaştırılmıştır.

Mikroyuvarların yüksek nitelik katsayılı çınlamalarının özenli kurgulanması ile, mikroyuvar ve dalgakılavuzlarındaki elmas azot boşluk (NV) özeklerin doğrusal olmayan özelliklerinin kullanılması, tüm bileşenleri elmas olan düzeneklerin gelecekte tümleşik elmas fotonik uygulamalarda kullanılmasını sağlayabilir.

ACKNOWLEDGEMENTS

I would like to express my profound gratitude to my advisor Professor Ali Serpengüzel for his kindness, guidance, and generous help throughout my Master of Science thesis research, and giving me the opportunity to work in Koç University Microphotonics Research Laboratory. I would like to deeply thank Professor Mehmet Burçin Ünlü, and Associate Professor Kaan Güven for participating to my MSc thesis committee, and their valuable feedback.

I would also like to thank Koç University Microphotonics Research Laboratory members and friends; Dr. Ulaş Sabahattin Gökay, Dr. Muhammad Zakwan, Muhammad Rehan Chaudhry, Syed Sultan Shah Bukhari, Mustafa Mert Bayer, Hüseyin Ozan Çirkinoğlu, Suat Kurt, and Yiğit Uysallı for their help in the laboratory, and for the discussions we had.

I would also like to thank our collaborators in Politecnico di Milano and Institute for Photonics and Nanotechnologies, Professor Roberta Ramponi, Dr. Shane Michael Eaton, Dr. Belén Sotillo, and Dr. Vibhav Bharadwaj for providing the shallow waveguide femtosecond laser written waveguides.

In addition, I wish to express my sincere gratitude to my dearest friends, Hande Karagöz, Pelin Livan, Cemre Göç, Yağmur Rumeli, Büşra Harmanda, Nihal Albayrak, Cem Bahadır Aksoy, İpek Kızıl, Elif Bedir, Vahdet Ünal, Jannatul Mawa, and Serap Aldemir, who have always supported me along the way with unforgettable memories.

For their endless love and support throughout in my life, I would like to thank my dear parents; Halime and İsmail Yavuz, my beloved sister, Halenur Yavuz Kienle, and her husband, Nickias Kienle. This accomplishment would not have been possible without them. Thank you.

Dedicated to my family

TABLE OF CONTENTS

List of Tables

List of Figures

NOMENCLATURE

a	radius of sphere
α	attenuation coefficient
b	impact parameter
B	root mean square (rms) length of surface inhomogeneities on the microsphere
c	speed of light in vacuum
D	diameter of sphere
F	finesse of cavity
h	Planck's constant
L	Fabry-Pérot cavity length
λ	incident wavelength in vacuum
λ_n	resonant wavelength in vacuum
λ_{FWHM}	full width at half maxima (FWHM) in wavelength
$\Delta\lambda_{FSR}$	free spectral range (FSR) in wavelength
$\Delta\lambda_n$	mode spacing in wavelength
m	relative refractive index
n	mode number
N	refractive index of the resonator
$N_{outside}$	refractive index of the outside medium
NA	numerical aperture of a lens
$\Delta\nu_{FSR}$	free spectral range (FSR) in frequency
$\Delta\nu_n$	mode spacing in frequency
Q	quality factor of a resonance
Q_{int}	quality factor associated with the internal losses
Q_{rad}	quality factor associated with the radiative losses
Q_{cont}	quality factor associated with the surface contaminant losses
Q_{mat}	quality factor associated with the bulk material losses

Q_{ext}	quality factor associated with the external losses
Q_{coup}	quality factor associated with the coupling losses
Q_{tot}	total quality factor
R	reflectance
σ	root mean square (rms) size of surface inhomogeneities
t	time
$\left\|t^2\right\|$	incident mode intensity coupling coefficient
T	absolute temperature
τ	lifetime of photon inside cavity
θ_i	incidence angle
θ_t	transmittance angle
θ_c	critical angle
x	size parameter of microsphere

Chapter 1

INTRODUCTION

Whispering gallery modes (WGMs) were first observed in sound waves by Sir Lord Rayleigh in the first years of 20th century in St. Paul's cathedral [1]. Sound waves, fitted in a circular structure, exhibit resonance condition based on the reflection of sound from the walls. Similarly, this phenomenon occurs in light waves trapped inside an optical cavity by total internal reflection (TIR), known as whispering gallery modes (WGMs), a subset of morphology dependent resonances (MDRs). Cavities, that support such WGMs or MDRs, are called resonators. Until now, materials such as silica (SiO_2) [2], silicon (Si) [3], lithium niobate ($LiNBO_3$) [4], diamond [5], and liquid droplets [6] are used in geometries such as rings [7], discs [8], spheres [9], and toroids [10] to realize WGM microcavities. The combination of such materials with the WGM microcavities is vastly investigated due to the resulting unique optical and electrical properties of such a combination. Previously, resonances from microresonators such as Si [11], SiO_2 [12], and diamond [13] were harvested for optical filtering [14], channel dropping [15], lasing [16], and sensing [17] for applications such as tunable optical channel add-drop filters [18], laser resonators [16], and WGM biosensors [17].

We choose silicon and diamond spherical microcavities, since these group IV materials enhance high quality factors in quite small modal volumes with their high refractive indices. Both materials hold significant interest for integrated photonics industries. Silicon, the standard material of complementary metal-oxide-semiconductor (CMOS), is also a highly selected component for photonic integrated circuits (PICs), as it provides high refractive index contrasts in the applications of optical amplifiers and modulators [19], as well as photonic crystal waveguides [20]. Diamond is used for photonics applications in Raman lasers [21], photonics waveguides and cavities [22], as it has marvelous optical, thermal, and chemical properties [23].

Silicon (Si) and silica (SiO_2) are the most fundamental optical components in optical fibers, optical filters, optical amplifiers, photodetectors in integrated optical devices, and photonic integrated circuits (PICs) [24].

Moreover, to realize high Q-factor resonances, it is essential to achieve a superb coupling of light from a guiding propagation medium such as tapered fibers [12], prisms [25], optical-fiber-half-couplers (OFHCs) [26], and optical waveguides [27] to the smooth curvature of the microsphere. The high optical transparence in infrared wavelength region makes, silica, such as Gorilla and Eagle$^{2000™}$ glasses, one of the most fundamental optical waveguide materials for evanescent light coupling to the WGMs of silicon and diamond microspheres [27].

Applications in quantum regime have been rapidly developing, and there is a continuous search for a suitable and faster photonics platform as successful as silicon [21]. Having outstanding mechanical properties like hardness, high thermal conductivity, chemical inertness [28], as well as unique optical properties, such as high Raman gain, possible nonlinear behaviors triggered by nitrogen vacancy (NV) centers, large energy difference between valance and conduction bands (5.5 eV), and wide transmission window from ultraviolet (UV) to far infrared (far-IR) points out diamond as a promising photonic platform for optical filtering, sensing, amplification [13], and various quantum realm applications [21].

The broadband transparency of diamond, with a refractive index of 2.38 [29] in near-IR, facilitates the observation of WGMs via integrating a photo-inscribed diamond waveguide (WG) with a diamond microsphere. WGMs manifest themselves by exploiting TIR due to the difference of refractive index between the external medium and the circular microcavity, where the circumnavigating light realizes a localization around the microsphere [30]. As is well known, these localized modes exhibit high quality factor (Q-factor) resonances inside small spherical cavities.

It was previously demonstrated that, fs-laser written silica WGs have capability of triggering high Q-factor WGMs inside Si microcavities with high impact parameters, while exhibiting a polarization selective response for transverse electric (TE) and transverse magnetically (TM) polarized lights [27]. Femtosecond (fs) laser photo-inscription technique enables diamond to function as a WG for photonic integration to diamond sphere to achieve an all diamond optical platform [31]. Additionally, it is possible to excite the Fabry-Pérot (FP) resonances in the

transmission direction in the WG, which will further yield an integrated FP resonator along with a spherical resonator for the combined diamond system.

In this work, we examine elastic scattering of 1 mm Si sphere excited by three different shallow waveguides inscribed by fs-laser on Gorilla Type I glass, Eagle$^{2000™}$ glass, and Type IIa (Nitrogen ~ 100 ppb) diamond. Lastly, we demonstrate a novel approach, an all diamond system, which performs excitation of a Type Ib (Nitrogen > 5 ppm) 1 mm diamond sphere via a Type IIa fs-laser written shallow diamond WG.

Chapter 2

WAVEGUIDES AND MICROSPHERE RESONATORS

2.1 Waveguide Parameters

A spatially inhomogeneous optical waveguide is employed for confining and guiding the electromagnetic wave forward along its propagation axis. Light is confined in the waveguide by using total internal reflection (TIR), which is governed by Snell's law, as in below Eq. 1;

$$N_1 \sin\theta_i = N_2 \sin\theta_r \tag{1}.$$

Figure 2.1 is an illustration of the light propagating in a denser medium (N_2), changing its direction depending on its angle of incidence (θ_i), when facing a less dense medium (N_1). When the reflected ray continues to propagate through the surface, that is, if its angle (θ_r) is equal to 90°, the incidence angle of the incoming ray is known to be the critical angle, as shown in Eq. 2. Moreover, the rays having incidence angles, which hold $\theta_i > \theta_{critical}$ encounter TIR.

$$\theta_{critical} = \sin^{-1}\frac{N_2}{N_1} \tag{2}.$$

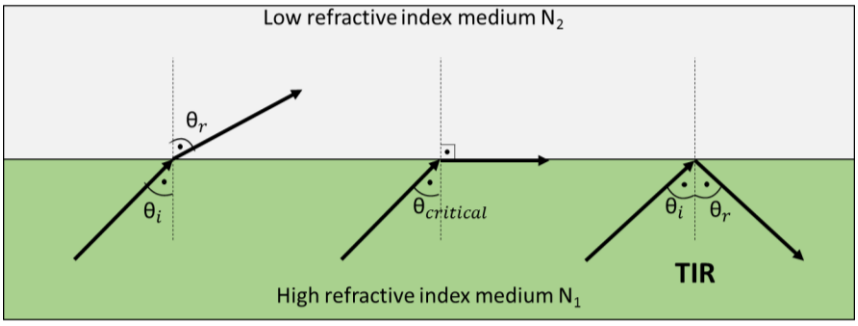

Figure 2.1: Illustration of total internal reflection (TIR) of a ray.

There are several different types of waveguides, according to their geometries, refractive indices, materials, and usage areas, e.g., planar, rectangular, cylindrical, and photonic crystal [32]. As one of the most common example of light confining by such phenomena, the Fabry-Pérot interferometer consists of two semi-transparent parallel mirrors, which trap the light with a phase matched round-trip between the mirrors [33]. A light beam incident with an arbitrary angle to the surface normal will undergo reflections and transmission over the mirrors, which have a fixed distance L, and the medium between the mirrors having a refractive index *N*, as indicated in Figure 2.2.

The mode number *n* of the roundtrip of the light trapped inside the mirrors is found using the following equation [34];

$$n\lambda = 2LN \quad (3),$$

and the resonance condition occurs, when there is integer number *n* of roundtrips, leading to a standing wave formation.

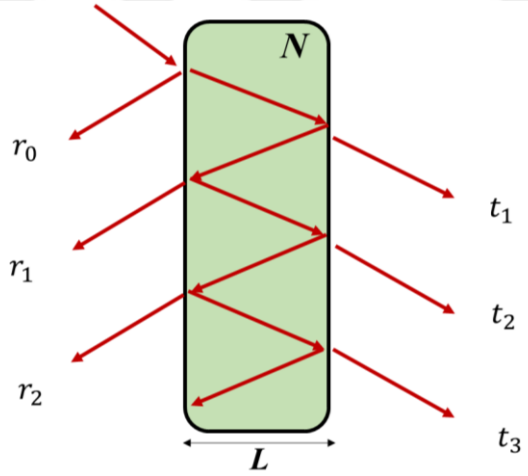

Figure 2.2: Schematic of the Fabry-Pérot interferometer.

The resultant spectra will have significant resonant peaks at corresponding wavelengths λ with mode numbers *n* due to the constructive interference of the wave inside the cavity. The distance between two consecutive resonant peaks is recognized as the free spectral range (FSR), and can be formulized in terms of frequency as;

$$\Delta \nu_{FSR} = \Delta \nu_{n+1} - \Delta \nu_n = \frac{c}{2LN} \quad (4),$$

where, c is the speed of light in vacuum, and n and $n+1$ indicate the consecutive mode numbers. Eq. 4 may also be written in terms of wavelength as in Eq. 5,

$$\Delta \lambda_{FSR} = \frac{\lambda}{\nu} \Delta \nu_{FSR} = \frac{\lambda^2}{2LN} \quad (5),$$

where λ is the central wavelength of the beam. It is clear that, a change in the length and/or the refractive index of the Fabry-Pérot resonator affect the FSR of the spectra, which proves that Fabry-Pérot resonators are sensitive to wavelength selection, and this motivates various applications for sensors and laser cavities [35].

Nonetheless, the sharpness of the defined resonant peaks characterizes the resolving power of the resonator. The quality factor of the resonance is determined by from the ratio between the resonant wavelength, and the full-width-at-half-maxima (FWHM) of the resonance peak shown as:

$$Q = \frac{\lambda}{\lambda_{FWHM}} \quad (6),$$

where λ_{FWHM} represents the FWHM of the peak.

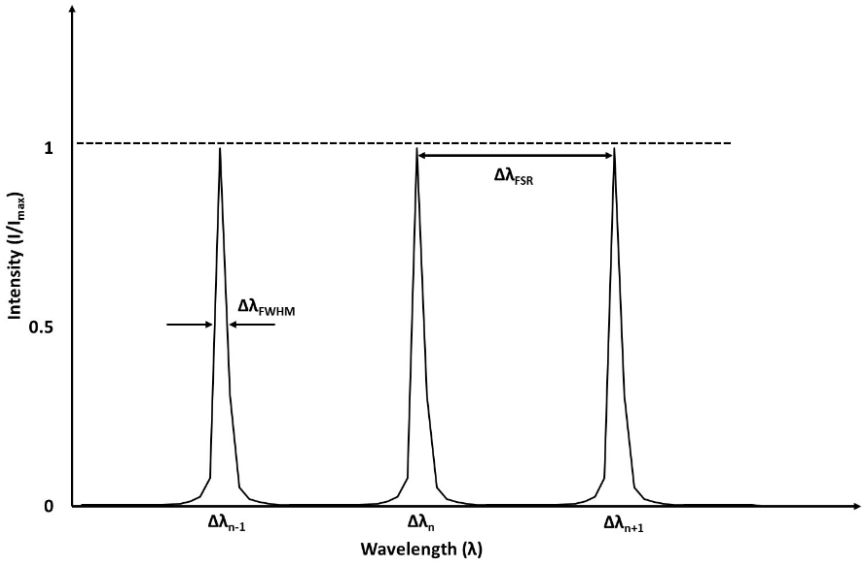

Figure 2.3: Schematic of a Fabry-Pérot resonator transmittance spectrum.

Figure 2.3 is an illustration of a sample transmission spectrum of a Fabry-Pérot resonator as $\Delta\lambda_{n-1}$, $\Delta\lambda_n$, and $\Delta\lambda_{n+1}$, represents the consecutive modes, $\Delta\lambda_{FSR}$ the distance of the consecutive peaks, and $\Delta\lambda_{FWHM}$ the FWHM of the resonance peak.

The finesse (F) of the resonator can be also obtained using Eq. 7, which shows the quality of a resonance, by taking the ratio of the FSR to the FWHM of the resonant peak.

$$F = \frac{\Delta\lambda_{FSR}}{\Delta\lambda_{FWHM}} \tag{7}.$$

More specifically the finesse for an ideal Fabry-Pérot resonator is defined by;

$$F = \frac{\pi\sqrt{R}}{1-R} \tag{8},$$

where R represents the reflectance of the mirrors in the cavity. High finesse Fabry-Pérot resonators provide strong light confinement inside the cavity, since F is independent from the length of the cavity, and is only determined by the losses, leading to various application areas in spectroscopy [36]. Eq. 9 defines the relation between the reflectance R of a Fabry-Pérot resonator parameters, and overall Q-factor of the resonator. As can be understood from the equation, the size parameter and the relative refractive index of the resonator are directly affecting the quality factor.

$$Q = \frac{\lambda}{\Delta\lambda_{FSR}} F = nF = \frac{2LN\pi\sqrt{R}}{\lambda(1-R)} \tag{9}.$$

2.2 Microsphere Parameters

Due to their morphology, microspheres support whispering gallery modes (WGMs), by exploiting consecutive TIRs inside its cavity, similar to Fabry-Pérot resonators, due to the difference of refractive index between the external medium and the circular cavity, where the circumnavigating light realizes a localization around the microsphere [30]. This is shown in Figure 2.4, where $N_{outside}$ is the refractive index of the outside medium, N the refractive index of the microsphere, a the radius of the microsphere, and θ_i the angle of the reflected ray.

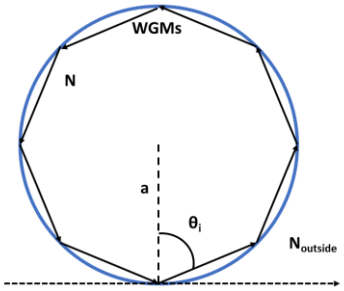

Figure 2.4: Illustration of a WGMs propagation inside a microsphere.

In spherical microresonators, some limitations like the size parameter and the impact factor need to be met in order for the beam to complete a one full roundtrip. The size parameter is a dimensionless ratio between the size of the sphere, and the operation wavelength λ such as [37]:

$$x \equiv ka = \frac{2\pi a}{\lambda / N_{outside}} \quad (10),$$

where a represents the radius of the sphere.

Furthermore, this size parameter can also indicate the relation between the mode number n of the spherical resonator for that wavelength. This limitation can be formulized such as:

$$x \leq n \leq Nx \quad (11),$$

where, N is the refractive index of the sphere, and the outside medium's refractive index is taken as 1.

As it is also described previously in the Fabry-Pérot resonator part, the distance between two consecutive resonant peaks is defined as an FSR. This distance can be also defined terminologically as the mode spacing for spherical resonators, since the range is not free like in the Fabry-Pérot resonator [38]:

$$\Delta\lambda_n = \frac{\lambda_n^{\,2} \tan^{-1}\sqrt{N^2-1}}{2\pi a\sqrt{N^2-1}} \quad (12),$$

where λ_n is the resonant wavelength, and refractive index of surrounding medium is taken as 1.

2.3 Microsphere WGM Spectra

A schematic figure of light coupling of a Gaussian beam to a spherical resonator can be seen in Figure 2.5. Here, the dashed line represents the center of the propagating transmission beam, *m* the relative refractive index, *k* the wavevector of the scattered light, *a* the radius of the sphere, and *b* the impact parameter, that is the distance between the center of the beam and the center of the sphere.

The impact parameter for coupling to a microsphere is restricted by $a \leq b \leq Na$ [39]. Only the incident beams in this impact parameter region can couple to the microsphere. Moreover, two different polarizations of light are used for our purposes: the transverse electric (TE) polarization, of which the electric field component is tangent to the surface of the sphere, and the transverse magnetically (TM) polarization, of which the magnetic field component is tangent to the surface of the sphere.

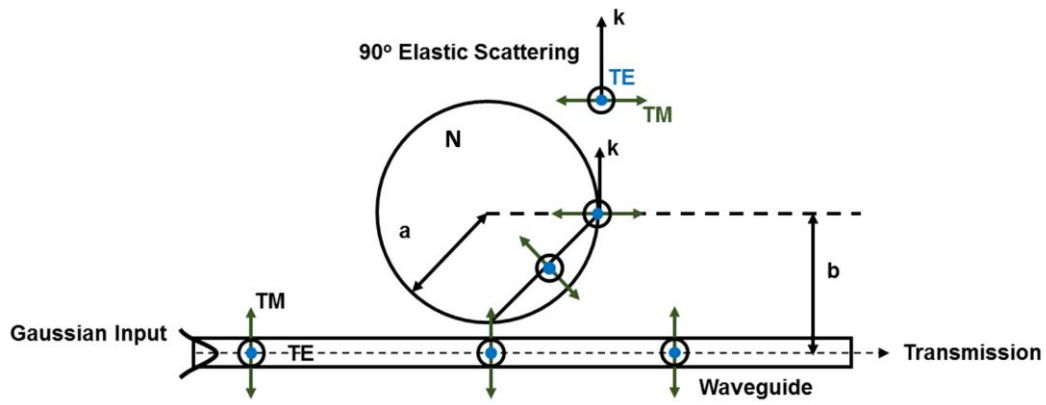

Figure 2.5: Illustration of coupling to a microsphere by a Gaussian beam.

Figure 2.6 is a drawing of the expected spectrum for both TE and TM polarized transmitted (blue curve) and scattered (red curve) light from the excitation source (in this case the waveguide) and scattered light from the resonator (in this case the microsphere). The dips of the transmission spectrum coincide with the peaks of the scattering spectrum, meaning that the particular wavelength completes the full roundtrip, which gives rise to a WGM. As discussed before, the gap between the dips in the transmission spectrum is the same as the gap between the peaks in the scattering spectrum (called as the FSR of the waveguide $\Delta\lambda_{FSR}$ in the Fabry-Pérot) is now called as the mode spacing $\Delta\lambda_n$ in the microsphere.

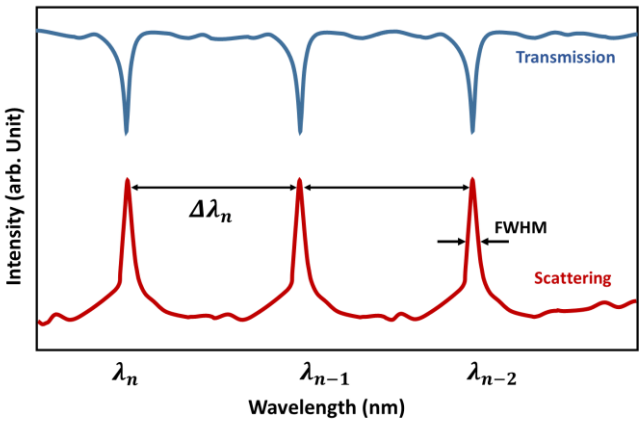

Figure 2.6: Drawing of the spectra for both transmission and scattering of light from a microsphere.

Using Eq. 13, the Q-factor, which defines the resolving power and sensitivity of the microresonator according to sharpness of a resonance peak, is calculated by the losses due to intrinsic radiative losses Q_{rad}, scattering losses Q_{ss}, surface contaminants Q_{cont}, material loss Q_{mat}, and the losses caused by the external light coupling Q_{ext} [40]:

$$Q_{tot}^{-1} = Q_{rad}^{-1} + Q_{ss}^{-1} + Q_{cont}^{-1} + Q_{mat}^{-1} + Q_{ext}^{-1} \quad (13).$$

Q_{rad} is the losses caused by the imperfections of TIR from curvatures [41], and Q_{cont} is the losses related with the surface contaminants, that may occur in the fabrication process of the microsphere. The scattering losses, $Q_{ss,}$ are due to the surface inhomogeneity, and estimated using the following [40];

$$Q_{ss} = \frac{\lambda^2 a}{\pi^2 \sigma^2 B} \quad (14),$$

where σ is the rms size, and B the correlation length of the surface inhomogeneity, are found to be < 2 nm. Q_{mat} is the losses material losses for atomic impurities, and the absorption of the material, and can be formulated as;

$$Q_{mat} \approx \frac{2\pi N}{\alpha\lambda} \quad (15),$$

where α is the attenuation coefficient for the material, that is used at that wavelength range, N is the refractive index of the material with respect to air as the outside medium.

The loss caused by the external light coupling is found by Eq. 16 [42]:

$$Q_{ext} = \frac{2\pi x}{\left|t^2\right|} = \frac{\left(2\pi\right)^2 a}{\lambda\left|t^2\right|} \qquad (16),$$

where t is the incident light mode field coupling coefficient, with generally $\left|t^2\right| << 1$.

Chapter 3

ELASTIC SCATTERING FROM Si SPHERE EXCITED BY FEMTOSECOND LASER WRITTEN GORILLA GLASS WAVEGUIDE

In this chapter, femtosecond (fs)-laser written Gorilla glass waveguide properties, mode profile of waveguides, Si sphere properties, experimental setup for excitation of WGMs from Si sphere, and finally experimental results are discussed.

3.1 Gorilla Glass Waveguide Properties

Figure 3.1 shows shallow waveguide writing in the bulk Corning, Gorilla glass by using Pharos Light Conversion fs laser at 300 fs pulse duration, 1030 nm wavelength, 500 kHz repetition rate. Laser light is focused using 0.42 NA objective, and 20-25 μm below the surface. No waveguide structure can be formed at the depths shallower than 25 μm, since the glass surface is ablated by the fs laser. The waveguides have a high transmission rate at 1550 nm with large mode field diameter (MFD). However, the waveguides are inscribed with different parameters to observe their efficiency of evanescent field coupling to microspheres. Table 3.1 and 3.2 shows the vertical and horizontal MFD single mode guiding with variation of writing speed (v) from 2, 5, 10, 15, 20 mm/s, and laser power (P) changed 325, 350, 375 mW while the depth kept constant.

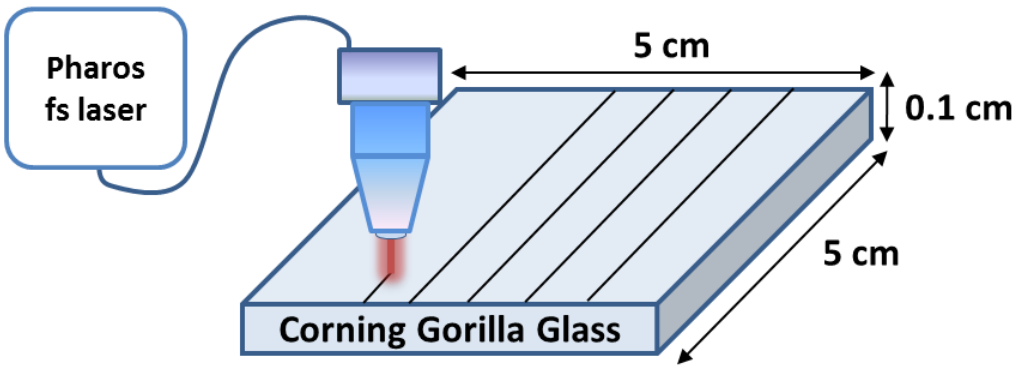

Figure 3.1 : Illustration of Gorilla glass inscription using Pharos fs laser.

Writing Speed v (mm/s)	Laser Power P (mW)		
	325	350	375
2	SM (17x21)	SM (17x22)	SM (19x26)
5	SM (18x22)	SM(17x22)	SM (18x23)
10	SM (21x24)	SM (19x23)	SM (19x24)
15	SM (24x27)	SM (21x24)	SM (19x24)
20	SM (28x30)	SM (22x26)	SM (20x24)

Table 3.1: MFDs of 20 µm depth waveguides with different writing speeds and laser powers.

Writing Speed v (mm/s)	Laser Power P (mW)		
	325	350	375
2	SM (17x21)	SM (17x22)	SM (18x25)
5	SM (19x23)	SM(16x19)	SM (19x25)
10	SM (21x26)	SM (19x24)	SM (20x25)
15	SM (25x28)	SM (21x25)	SM (21x25)
20	SM (29x32)	SM (23x27)	SM (22x26)

Table 3. 2: MFDs of 25 µm depth waveguides with different writing speeds and laser powers.

A 25 µm depth, 5 mm/s speed, 350 mW laser power written waveguide is chosen to observe the light coupling to silicon microsphere, shown in green in Table 3.2.

Figure 3.2 (a) and (b) show the SEM images of top view and side view of the chosen waveguide. Figure 3.2 (c) shows MFD as 16 µm vertical and 19 µm transverse directions as the near-field intensity profile of this waveguide at 1550 nm wavelength. This waveguide is inscribed with a 6.0 dB insertion loss, and 0.8 dB/cm propagation loss. Gorilla glass waveguides used for evanescent field light coupling to Si microsphere in this project, because fs-laser inscribed Gorilla glass waveguides have large MFD with single mode propagation suitable for near-IR light coupling to the Si sphere.

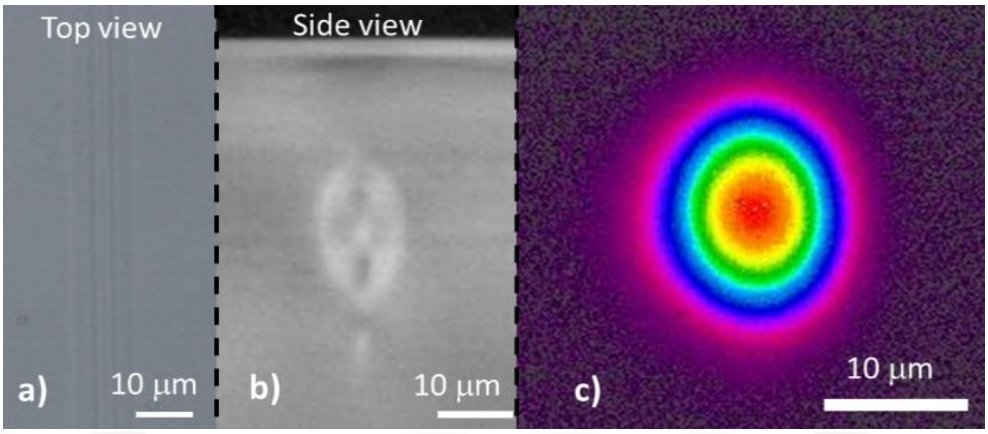

Figure 3.2: a) Top b) end view c) near field intensity profile of the fs-laser written Gorilla waveguide.

3.2 Gorilla Glass Waveguide Mapping

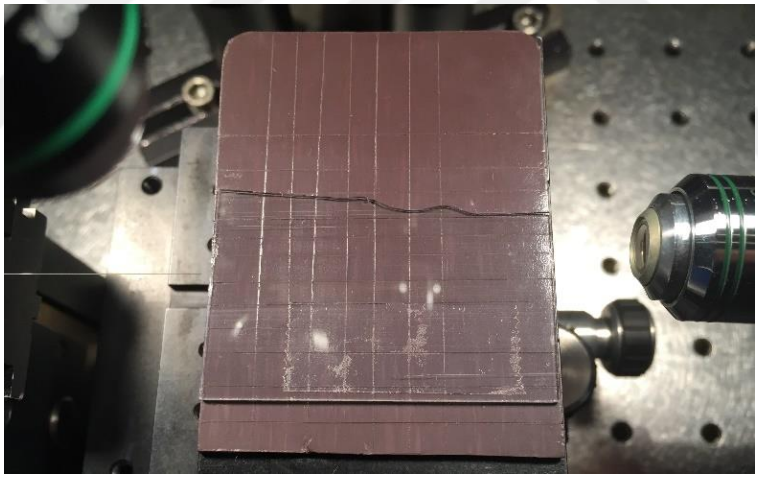

Figure 3.3: Femtosecond laser written Gorilla glass waveguides.

Figure 3.3 is the image of the Gorilla glass waveguide sample placed on brown platform of the micrometer stage. A pigtailed bare fiber carries the light to the waveguide at the left side of the glass, and the output is detected from the right side of the waveguide end by a 20X, 0.40 NA Edmund Optics objective, which is connected to a webcam through 10X eyepiece.

Figure 3.4 shows the experimental setup for characterizing the fs-laser written waveguides, and observing the output of the beam profile of the waveguide. An OZ Optics red probe laser operating at 637 nm is used as the light source propagating through the waveguides.

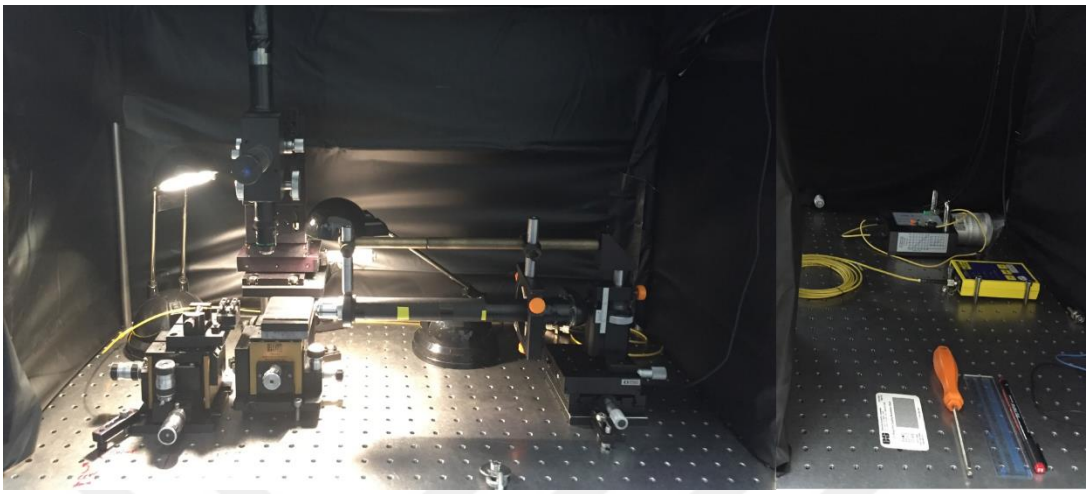

Figure 3.4: Experimental setup for mapping the output of the Gorilla glass waveguides.

Figure 3.5 indicates the beam profiles of five waveguides between the two ablation lines (ALs) with the insets showing their inputs by a single mode bare fiber. AL1 indicates the first ablation line, which is a nonguiding medium. The laser ablated regions are used to separate the waveguides of different writing depths. WG1, WG2, WG3, WG4, and WG5 indicate the first, second, third, fourth, and fifth waveguide after AL1 with scanning speed of 2, 5, 10, 15, and 20 mm/s, respectively.

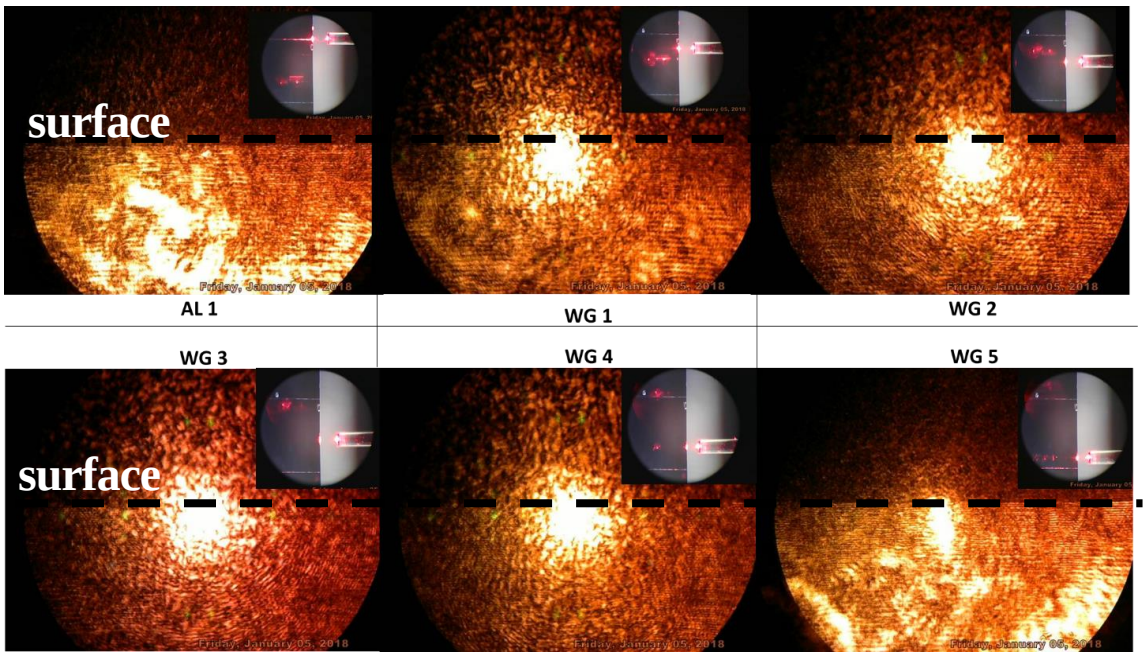

Figure 3.5 : 25 µm deep, 350 mW, different scanning speed written WG beam profiles. Insets are input top views.

Figure 3.6 is an illustration of the Gorilla glass waveguide for using it as a map for further studies. The inset of this figure shows the place of waveguides with different writing speeds between the two ablation lines. The waveguide used for our experiments is shown as an orange dashed line on the map.

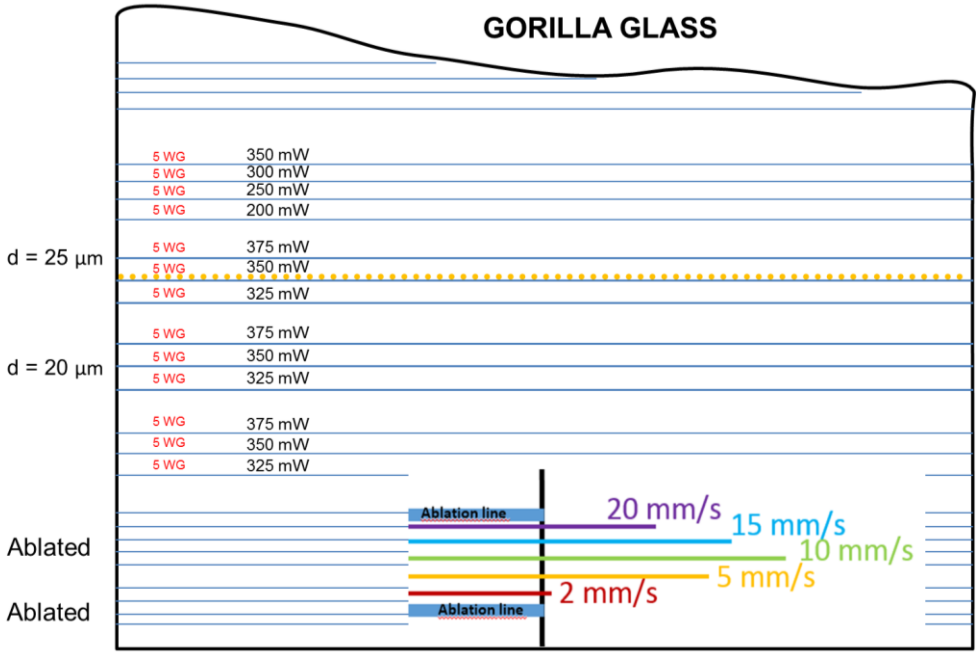

Figure 3.6 : Map of the fs-laser written Gorilla glass waveguides.

3.3 Silicon (Si) Sphere

Si microsphere purchased from Ball Semiconductor has ~1 mm diameter. The sphere was manufactured by process called crystallization of melted Si droplets facing a free-fall inside a plasma furnace. Then the sphere is mechanically lapped and polished, achieving an accurate form of mirror-like finish and round surface without defects [43]. The sphere is cleaned by an isopropanol and acetone mixture inside an ultrasonic bath to remove any surface contaminants before the experiment. Figure 3.7 is the visible camera image of the lapped Si sphere used for our purposes.

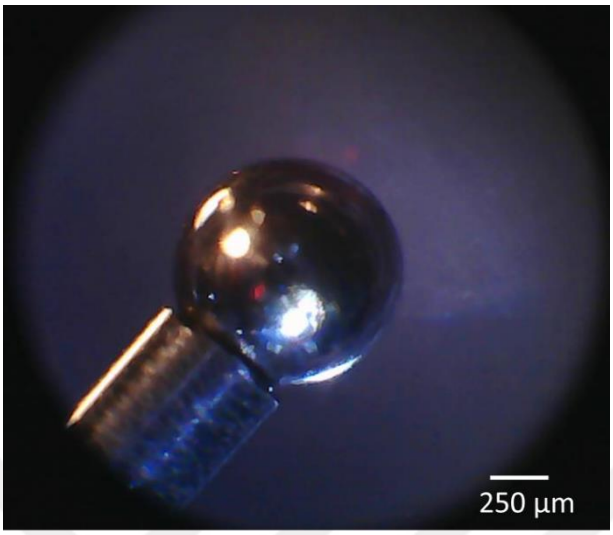

Figure 3.7: Lapped Si sphere 1 mm in diameter.

3.4 Experimental Setup

The experimental setup for coupling the infrared (IR) laser light to observe the WGMs of the Si sphere is shown in Figure 3.8. A Princeton Lightwave distributed feedback laser (DFB) laser is used as excitation source connected to ILX Laser Diode Controller to tune the narrow laser linewidth around 1427 nm with 1.1 pm spectral resolution. The continuous wave (CW) laser light transferred through a single mode (SM) bare fiber into the waveguide. Butt-coupled bare fibers and the Gorilla glass waveguide sample is placed on three dimensional translational stages in order to make the alignment precise. The optical fiber at the output end of the waveguide is connected to 50/50 Y-coupler to feed both the photodetector and the optical wavelength meter.

Elastic light scattering from both 0° angle transmission and 90° angle scattering were detected by InGaAs photodiodes (PDs). The detectors were connected to a 100 MHz bandwidth digital storage oscilloscope (DSO) via BNC connectors and the oscilloscope was connected to PC via IEEE-488 General Purpose Interface Bus (GPIB) to accumulate the data.

The 500 µm radius Si sphere is positioned by a metal needle tip connected to vacuum suction system and controlled with a three dimensional micrometer stage, as shown in Figure 3.9. A beam splitter was placed in an optical microscope T-tube in order to split the elastically scattered light collected by 10X microscope objective into two. A visible camera was placed at one end of the microscope T-tube

for imaging and placing the microsphere. InGaAs PD was placed on the other end of the microscope T-tube.

DSO, the diode laser controller and the optical multimeter (OMM) were connected to a PC via GPIB to control and acquire data using LabView (National Instruments) software program.

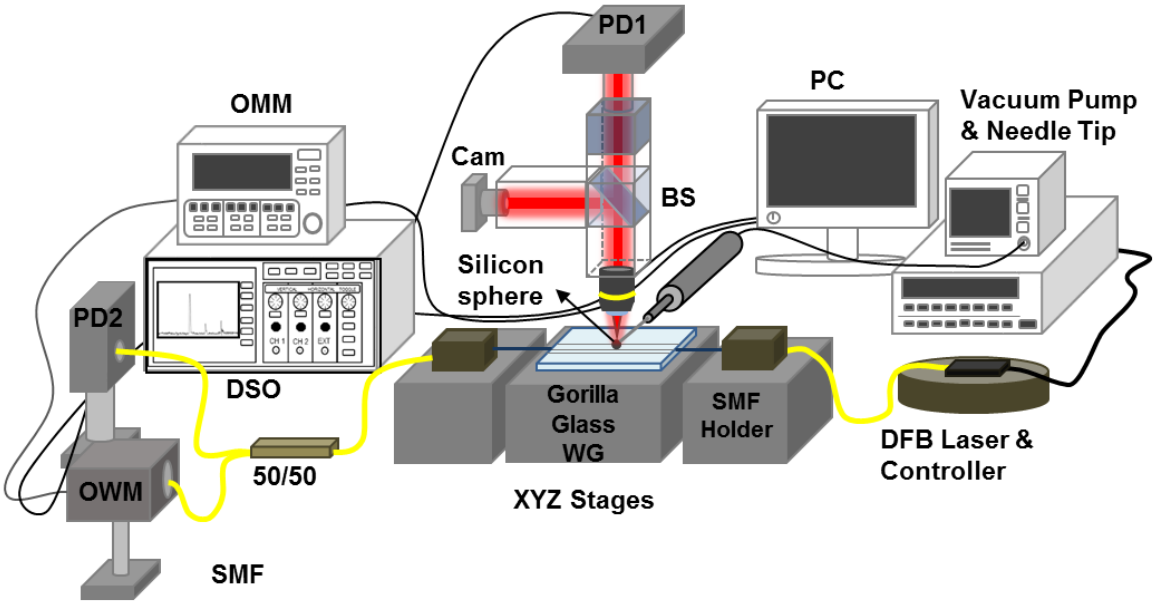

Figure 3.8: Experimental setup for light scattering of Si sphere on 25 µm deep fs-laser written Gorilla glass waveguide.

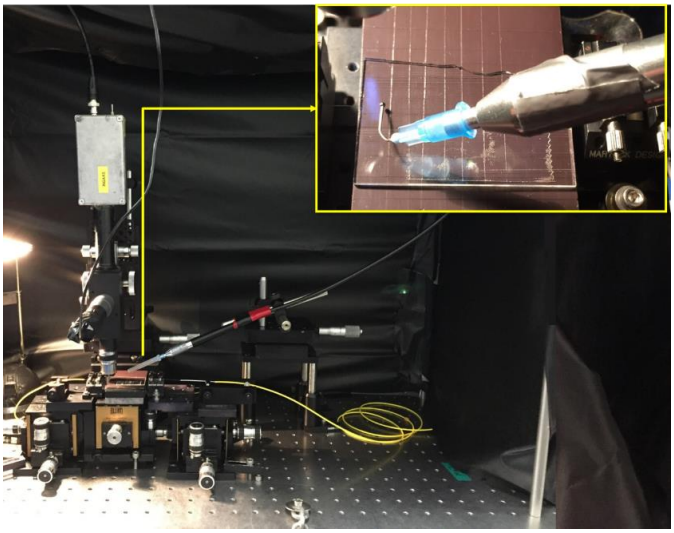

Figure 3.9: Elastic scattering from lapped Si microsphere on Gorilla glass waveguide experimental setup image.

3.5 Experimental Results

Figure 3.10 is the spectra of both 90° scattering and 0° transmission results for the lapped Si sphere excited by fs-laser inscribed 25 μm deep Gorilla glass waveguide. The mode families can be clearly seen from the spectra as the light couples to the 1-mm Si sphere. This is a satisfying result for understanding the coupling strength.

For this specific configuration, the mode spacing $\Delta\lambda$ is calculated to be 0.249 nm [44], according to Eq. 12. This mode spacing value correlates well with the value observed in the elastic scattering spectra with mode spacing of 0.25 nm, as it can be seen in Figure 3.11. The size parameter is estimated as $x \approx 2200$ at 1427 nm meaning that, Si sphere can support WGMS with a minimum $x \approx 2200$ up to $mx \approx 7660$ mode number, since the polar angular mode number n of the WGMs around the microsphere is restricted by $x \leq n \leq Nx$. The impact parameter for coupling to a microsphere is similarly restricted by $a \leq b \leq Na$ [39], which is in this case 500 μm ≤ b ≤ 1740 μm. Assuming the WG and the sphere are in contact, the impact parameter is $b \approx 525$ μm, satisfying the localization principle.

Experimentally the Q-factor is determined using $Q = \lambda/\delta\lambda$, where λ is the resonance wavelength and $\delta\lambda$ the full-width-at-half-maxima (FWHM) of the resonance. The narrowest peak has $\delta\lambda = 10$ pm FWHM, at a wavelength of 1426.9 nm, and the Q-factor of this peak is measured as 1.3×10^5.

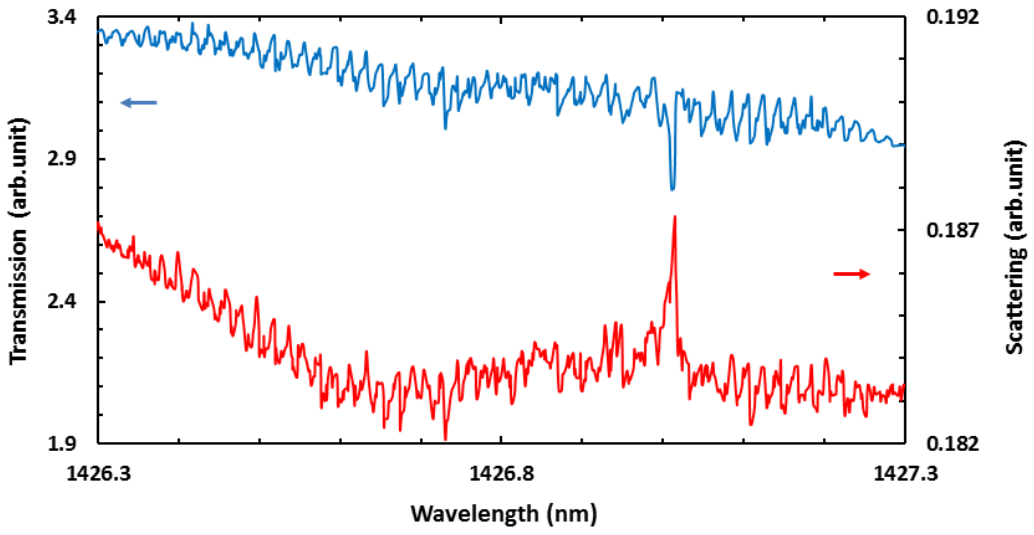

Figure 3. 10: WGMs in the scattering and transmission spectra from Si sphere on Gorilla glass waveguide.

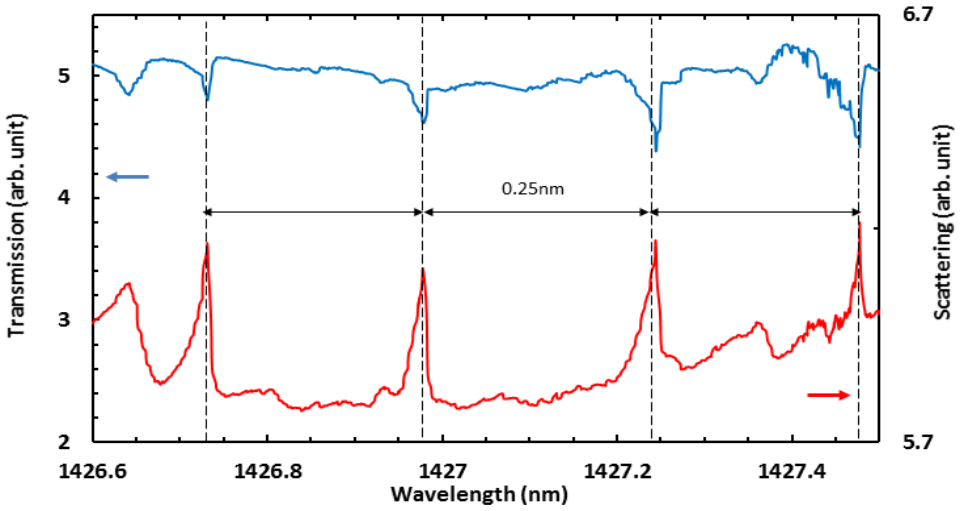

Figure 3. 11: WGMs in 0° transmission and 90° scattering of Si sphere using Gorilla glass waveguide.

Chapter 4

ELASTIC SCATTERING FROM Si SPHERE EXCITED BY FEMTOSECOND LASER WRITTEN EAGLE$^{2000™}$ GLASS WAVEGUIDES

4.1 Eagle$^{2000™}$ Glass Properties and Waveguides

Corning® Eagle$^{2000™}$ glass as an alkaline earth borosilicate, has refractive index of 1.5, density of 2.38 g/cm^3, low thermal expansion, clear in appearance, extraordinary optical properties as it shows extremely broad transmission percentage (above 90%) in the visible and near-IR wavelength regions of the electromagnetic spectrum [45]. Eagle$^{2000™}$ is supplanted by Eagle XG™, because of the need in the arsenic free glass type with the same qualities of Eagle$^{2000™}$, for use in several application areas like active matrix liquid crystal display (AMLCD), chips on glass (COG), and optoelectronics [45].

According to the transmission spectrum from 200 – 1100 nm of Eagle$^{2000™}$ glass of 0.7 mm thickness shown in Figure 4.1 [46], Eagle$^{2000™}$ shows excellent optical fidelity for light coupling from fs-laser written Eagle$^{2000™}$ glass waveguide to a microsphere, which is also transparent in the near-IR wavelength region.

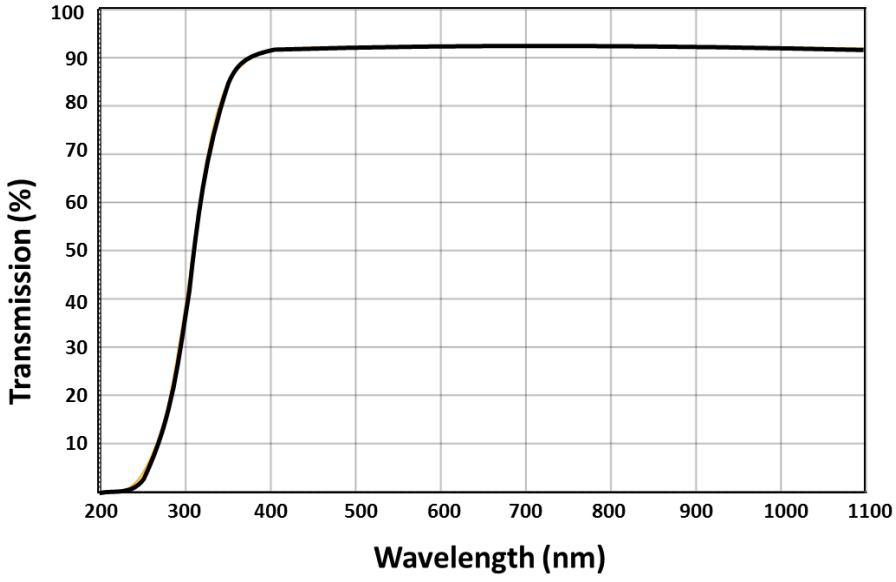

Figure 4.1: Transmission spectrum of Eagle$^{2000™}$ glass in UV, visible, and near- IR regions.

The waveguides are inscribed to an Eagle$^{2000™}$ glass 5 mm x 5 mm x1 mm sample, as it is described in Chapter 3.1. A Pharos Light Conversion fs laser at 300 fs pulse duration, 1030 nm wavelength, 1 MHz repetition rate is used for inscription laser tool to write the waveguides from 10 – 25 µm depths, while varying the laser power from 500 – 750 mW at 20 mm/s scanning speed for each depth. In Figure 4.2, (a) the map of the shallow waveguides written on Eagle$^{2000™}$ glass sample for our purposes, and (b) the list of the mode field diameter (MFD) of waveguides for specific depths and powers of the inscription laser is shown. The waveguide, at a 20 µm depth, written by 550 mW laser power, is a good candidate for evanescent field light coupling, since it has the optimum single mode MFD of 24 µm x 27 µm. This waveguide can be seen in Figure 4.3, together with the ablation lines (which are boldly visible), manufactured during the inscription due to the limits of their related laser power and the depth.

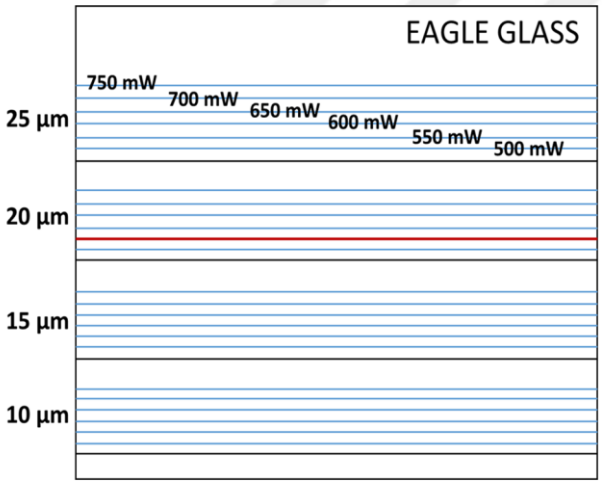

a)

Laser Power (mW)	Waveguide Depth (µm)			
	10	15	20	25
500	Ablated		16 µm x 17 µm	14µm x 15 µm
550	Ablated		24 µm x 27 µm	15 µm x 17 µm
600	Ablated		Ablated	16 µm x 19 µm
650	Ablated		Ablated	26 µm x 34 µm
700	Ablated		Ablated	Ablated
750	Ablated		Ablated	Ablated

b)

Figure 4.2: (a) fs-laser written Eagle$^{2000™}$ glass waveguide map, (b) MFD of these waveguides.

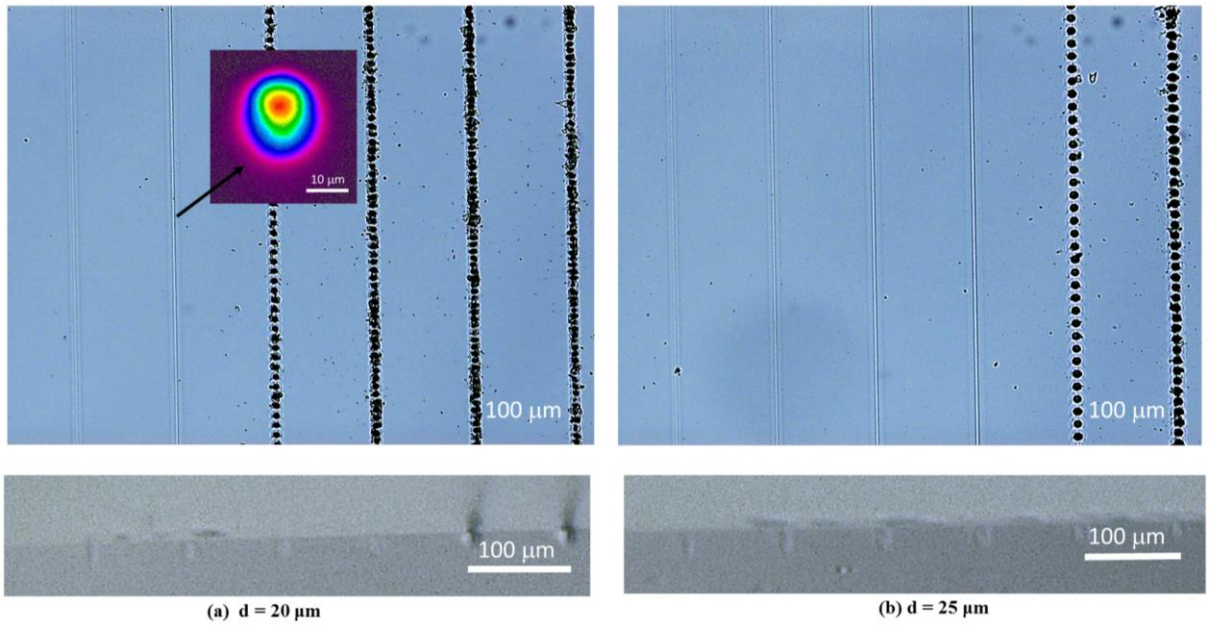

Figure 4. 3: Microscope images of waveguides at (a) 20 µm and (b) 25 µm depth. Inset is the MFD of the selected waveguide.

4.2 Experimental Setup for Silicon Sphere Scattering from Eagle Waveguide

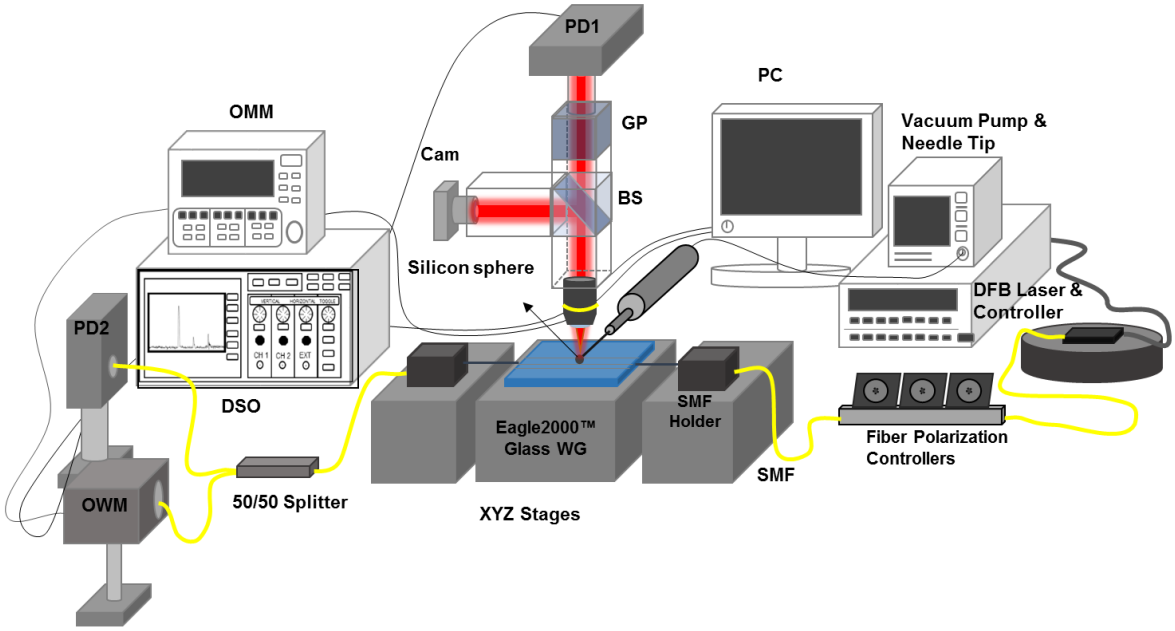

Figure 4. 4: Experimental setup for scattering from Si sphere on 20 µm deep fs-laser written Eagle$^{2000™}$ waveguide.

In this experiment, the same lapped Si sphere was used as discussed in Chapter 3.3, as shown in Figure 3.7: Lapped Si sphere 1 mm in diameter The Si sphere is placed on the waveguide with a drop of index matching gel (Thorlabs, #G608N), which has refractive index of 1.46. The experimental setup for coupling TE and TM polarized infrared (IR) laser light to Si sphere is shown in Figure 4. 4. A Princeton Lightwave distributed feedback laser (DFB) laser is used as the excitation source connected to ILX Laser Diode Controller to tune the laser with a narrow linewidth around 1427.5 nm. Continuous wave (CW) laser light is transferred through a single mode (SM) bare fiber through a manual fiber polarization controller to the Eagle glass waveguide. The paddles of the polarization controller act like waveplates to change the stress induced birefringence inside the wrapped fibers around the three spools. Hence, the polarization of the transmitted light can be changed inside the SMF.

Butt-coupled bare fibers are aligned to the Eagle$^{2000™}$ glass waveguide sample, which itself is placed on three dimensional translational stages for precise alignment. The fiber at the output end of the waveguide is connected to a 50/50 Y-coupler to feed the output to both the photodetector and the optical wavelength meter.

Elastic light scattering from both polarizations of light at 0° angle transmission and 90° angle scattering were detected by InGaAs photodiodes (PD 1 & PD 2). The detectors were connected to a 100 MHz bandwidth digital storage oscilloscope (DSO) via BNC connectors and the oscilloscope was connected to PC via IEEE-488 General Purpose Interface Bus (GPIB) to accumulate the data.

500 μm radius Si sphere, positioned by a metal needle tip connected to vacuum suction system, is controlled with a three dimensional micrometer stage. A beam splitter (BS) was employed to divide the collected light into two arms; one arm for visible optical camera (cam), the other for the PD2. In order to select the polarizations of the scattered light, a Glan polarizer (GP) is used.

DSO, the laser diode controller, and the optical multimeter (OMM) were connected to a PC via GPIB to control, and acquire the data using LabView (National Instruments) software program.

4.3 Experimental Results

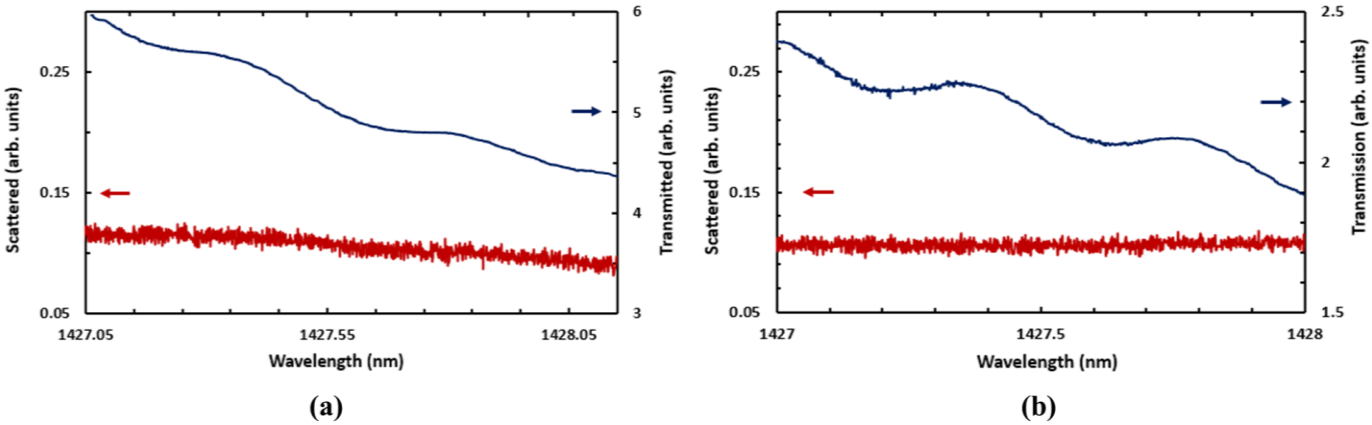

Figure 4.5: 0° transmission and 90° (a) TE and (b) TM polarized scattering spectrum without the silicon sphere.

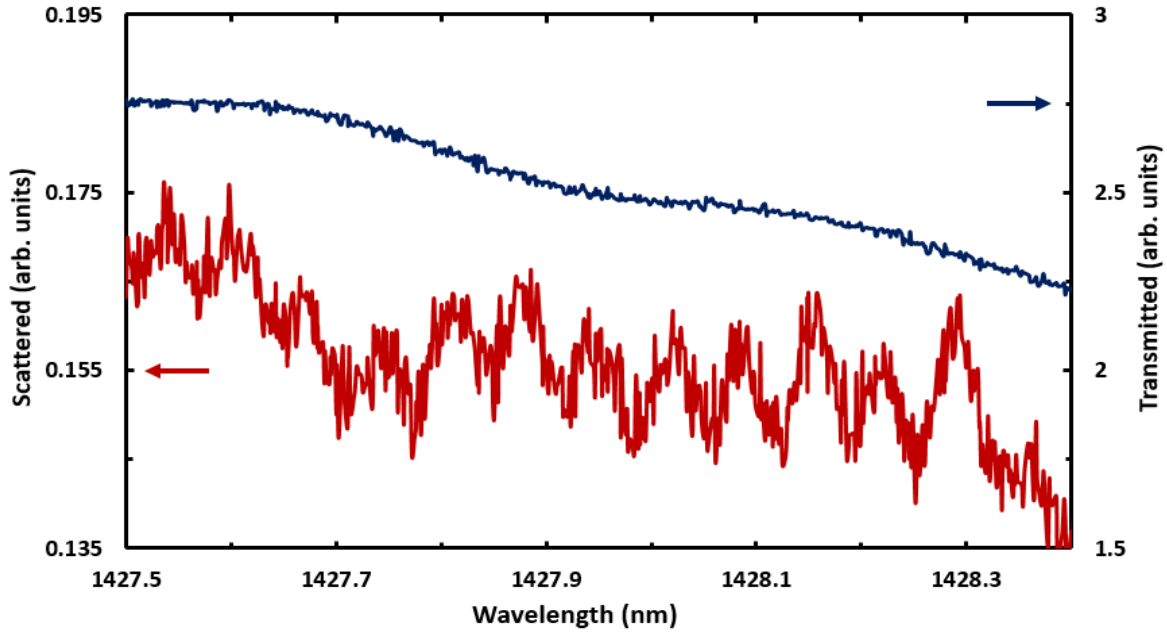

Figure 4.6: 0° transmission and 90° TE polarized scattering from the Si sphere using Eagle^{2000TM} waveguide.

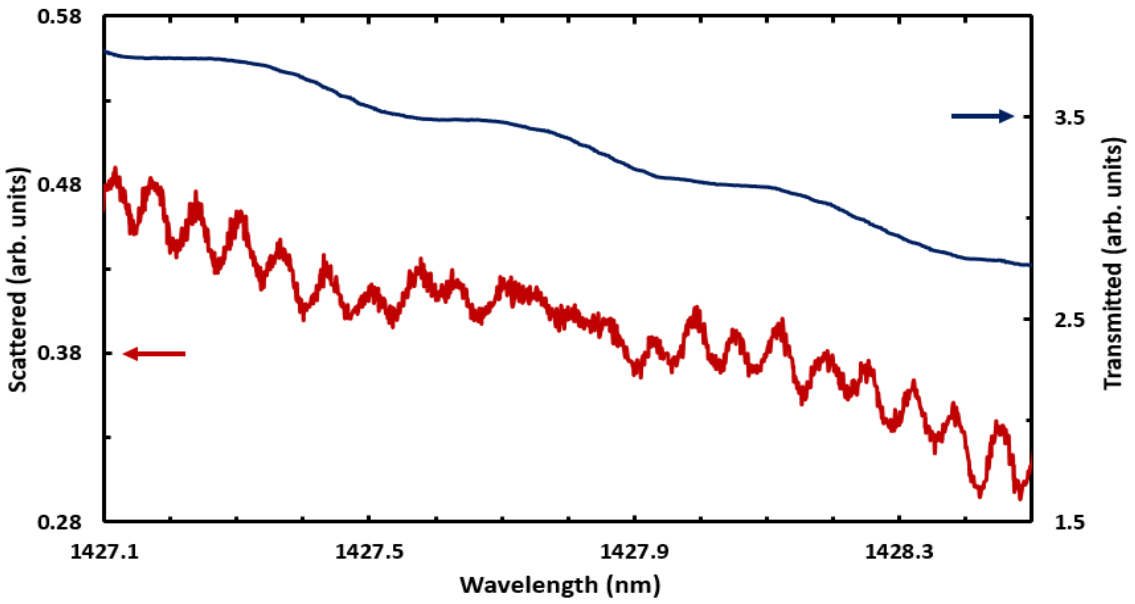

Figure 4. 7: 0° transmission and 90° TM polarized scattering from the Si sphere using Eagle$^{2000™}$ waveguide.

TE and TM polarized 90° elastic scattering (shown as the blue curves) and 0° transmission (shown as the red curves) spectra of the resonances of the 1 mm silicon sphere excited by a 20 μm depth shallow waveguide for 1 nm wavelength sweep, from 1427 nm to 1428 nm shown in the Figure 4.6 and Figure 4.7 respectively. The mode families can be clearly seen from the spectra as the light coupled to 1-mm Si sphere. The size parameter is estimated as $x \approx 2200$ at 1427.5 nm. The Si sphere can support up to $mx \approx 7660$ mode number, since the polar angular mode number n of the WGMs around the microsphere are restricted by $x \leq n \leq Nx$, and adequate for our case, as also recognized in Chapter 3.5. The impact parameter for coupling to a microsphere is restricted by $a \leq b \leq Na$ [39]. Only the incident beams in this impact parameter region could couple to the microsphere. For our experiment, assuming the WG and the sphere are in contact, the impact parameter is $b \approx 520$ μm, satisfying the localization principle. Experimentally the Q-factor is determined using $Q = \lambda/\delta\lambda$, where λ is the resonance wavelength and $\delta\lambda$ the full-width-at-half-maxima (FWHM) of the resonance. The narrowest peak has $\delta\lambda = 26$ pm FWHM, at a wavelength of 1427.26 nm and the Q-factor of this peak is measured as 5.5×10^4 for TM polarized spectra. For TE polarized spectra the narrowest peak has $\delta\lambda = 26$ pm FWHM, at a wavelength of 1427.64 nm and the Q-factor of this peak is measured as 5.4×10^4, correlate very well with the TM polarization results.

Chapter 5

ELASTIC SCATTERING FROM SILICON AND DIAMOND SPHERE EXCITED BY FEMTOSECOND LASER WRITTEN DIAMOND WAVEGUIDES

In this chapter, optical properties of diamond, diamond sphere, diamond waveguide fabrication by fs laser, the experimental setup for WGMs observation of diamond and silicon microsphere excited by fs-laser written diamond waveguide and the results for these experiments will be discussed. The experiments performed on the same experimental setup for both silicon sphere and diamond sphere.

5.1 Properties of Diamond

Diamond is one of the allotropes of element carbon, which means the difference between graphite, and diamond is only their three dimensional atomic structure. In a diamond structure, a carbon atom is surrounded by covalently bonded four other carbon atoms, which makes it very unique and the hardest material known. Since the electrons of carbon atoms bonded with neighboring valance electrons, diamond exhibits a tetrahedral lattice structure. However, there may be several defects in the structure. Optically active defects in such a lattice structure are called color centers. For example, there may be impurities and holes in the structure or missing atoms in the structure, which are called as vacancies. The most common impurities are known as nitrogen vacancy (NV) centers [47]. Replacing two carbon atoms by one nitrogen and a vacancy leads to a NV center with a floating electron. Also known as point defects, NV centers have two types according to the charge of an unpaired electron in the vacancy, i.e., if the unpaired electron is neutral, it is known as NV^0, and if it is negatively charged, it is known as NV^-. The research on NV centers in diamond is rapidly growing, and the applications of diamonds getting prominent like solid state physics as a laser gain media [48], and quantum photonics as a platform for integrated photonic circuits [49].

5.2 The Diamond Waveguides

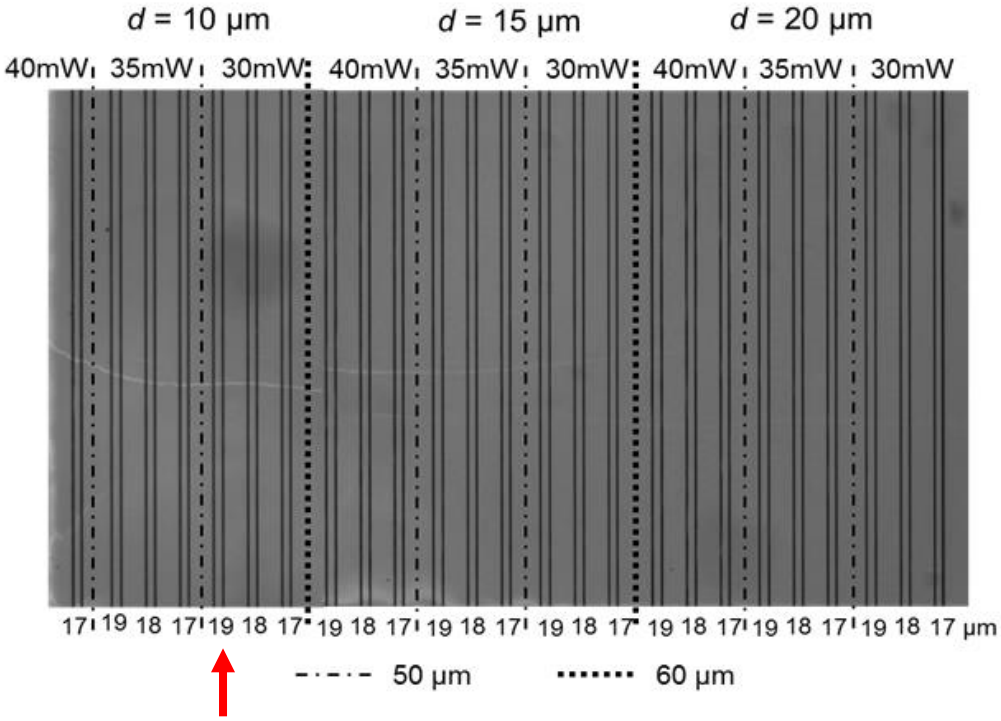

Figure 5.1: Microscope image of fs-laser inscribed diamond waveguides (waveguide with the red arrow was used).

Ultrashort pulsed lasers are becoming the most powerful tool for micromachining, since those lasers are very capable of generating high irradiances and optical breakdowns in transparent materials [50]. The type II fabrication technique is applied to achieve stress-induced lightwave guiding in between two parallel lines by inducing refractive index differences between the material and the lines using an inscription tool Pharos, Light Conversion amplified Yb:KGW pulsed laser operated at 515 nm, 500 kHz repetition rate, and 230 fs pulse duration [51]. Waveguides are micromachined to a Type IIa, nitrogen impurities of 100 ppm, synthetically grown diamond bulk material, which is polished for smooth planar surface with varying femtosecond laser powers, at different widths and depths to achieve the matching beam profile for light coupling to microresonator. Figure 5.1 is a map showing the depths, writing powers, spacing and widths of each waveguide written on the diamond sample [52]. The waveguides written at 10 – 30 µm deep with the increments of 5 µm, with the spacing of 17-18-19 µm, while the laser power changed between 30 – 40 mW with the increment of 5 mW, and

corresponding pulse energies of 60 – 80 nJ. The scanning speed is kept constant at 0.5 mm/s and the laser light is focused by 100X oil immersion microscope objective of 1.25 NA.

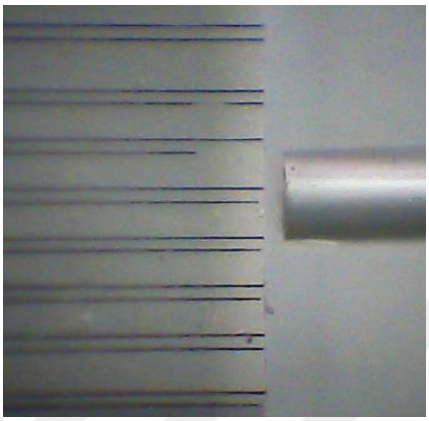

Figure 5. 2: The image of the used diamond waveguide. The butt-coupled bare glass fiber transmits the light source.

Figure 5.2 shows top view visible light camera image used waveguide with a butt-coupled optical SM glass bare fiber. The WG with the optimal yield was written with 30 mW laser power, and has a depth of 20 μm from the center of the beam propagating to the surface, and a width of 19 μm. The WG exhibits 9 dB insertion loss at telecom band, and has a mode-field-diameter (MFD) of 16 μm × 20 μm elongated in the vertical axis. The mode propagating within the high-performance WG and cross-sectional end facet of the fs-laser inscribed WG is shown in Figure 5.3 (a) and (b), respectively. Note that, relative intensity of mode profile is indicated from red (1) to violet (0).

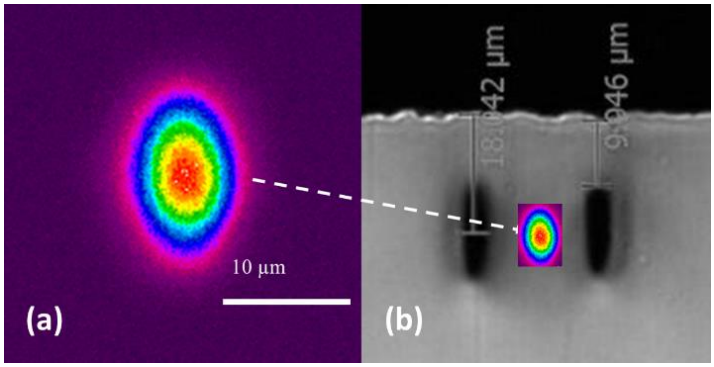

Figure 5. 3: (a) Color scaled MFD of the WG. (b) SEM of the WG end with the propagating beam profile.

5.3 Experimental Setup of Si and Diamond Spheres Excited by Diamond Waveguide

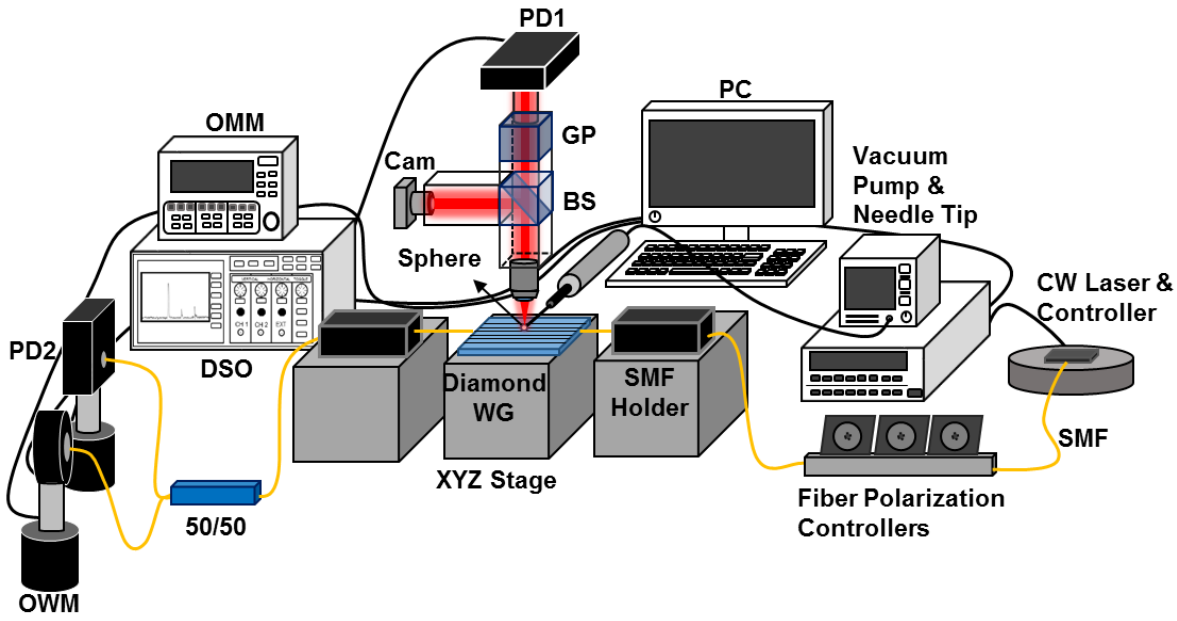

Figure 5.4: The schematic of the setup for scattering from Si and diamond spheres excited by diamond waveguide.

Illustration of the experimental setup for observing 90° elastic scattering and 0° transmission of TE and TM polarized near-IR region laser light, coupled to a 1-mm Si and diamond spheres by fs-laser written diamond waveguide is shown in Figure 5.4.

As an excitation source, a tunable continuous wave (CW) narrow linewidth Princeton Lightwave (PL) distributed feedback (DFB) laser is used. The DFB laser is controlled by an ILX Lightwave LDC 3744B Laser Diode Controller (LDC) with 1 pm resolution steps of fine temperature tuning around a central wavelength of 1427 nm. The laser light is transferred from the cleaved and polished end of an optical SM bare glass fiber with 8.2 μm core diameter to the waveguide entrance. Another fiber similar to the input fiber, is placed at the output of the WG to collect the transmitted light through the waveguide. The output is split into two by a 50/50 Y-coupler. One arm of the Y-coupler is directly connected by an FC/PC fiber connector to an InGaAs photodetector (PD1) for intensity measurements, and the other arm is directly connected by an FC/PC connector to the InGaAs optical

wavehead (OWH), which transports the information to ILX Lightwave OMM 6810B optical multimeter (OMM) to measure the light power and the wavelength. Another InGaAs photodetector (PD2) is placed on a microscope with a 20X magnification objective and an 10X eyepiece, which collect the elastically scattered light from the microsphere. Thus, both the transmission and the elastic scattering light acquired by the photodetectors are connected to a 100 MHz bandwidth digital storage oscilloscope (DSO) via BNC connectors. The oscilloscope is connected to a PC via IEEE-488 General Purpose Interface Bus (GPIB) to accumulate the data.

A beam splitter (BS) is employed to divide the collected light in to two arms: one arm for visible optical camera (cam), the other for the PD2. In order to select the polarizations of the scattered light a Glan polarizer (GP) is used before the 10X eyepiece. The 1 mm-diameter diamond sphere is brought to the close proximity of the waveguide surface by a vacuum pumped suction mechanism with a thin needle tip. The sphere is held from an equatorial position. DSO, LDC, and OMM are connected to a PC via GPIB to control and acquire the data using LabView (National Instruments) software program. This experimental setup is used for elastic scattering observation of both silicon and diamond spheres. Characteristics of the lapped Si sphere are explained in Chapter 3.3, and that of the diamond sphere are explained in Chapter 5.5.

5.4 Experimental Results for Si Sphere

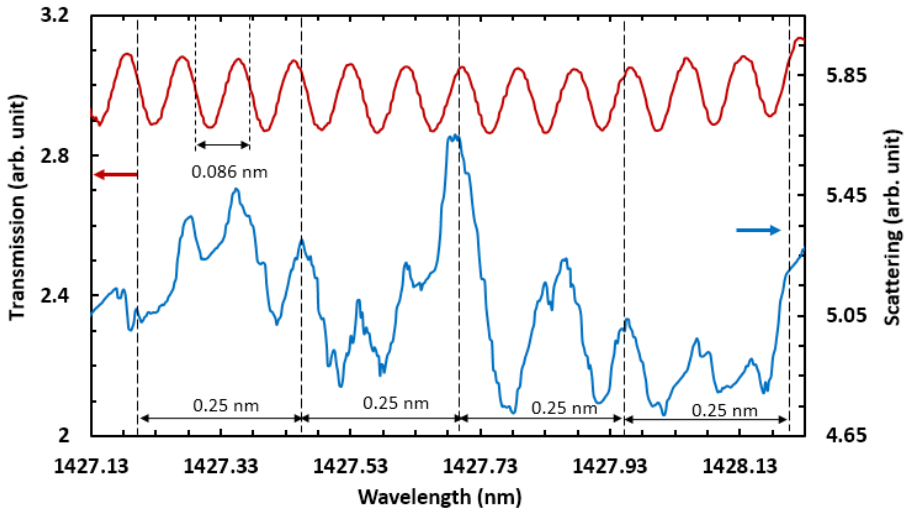

Figure 5.5: 0° transmission and 90° scattering from the Si sphere using diamond waveguide.

The resonance spectra, that is centered at around 1427.73 nm, for observation of elastic scattering from 1-mm Si sphere excited by fs-laser inscribed 20 μm depth shallow diamond waveguide, is shown in Figure 5.5. For the Si sphere having refractive index of 3.48 the calculated mode spacing, $\Delta\lambda$, between two consecutive mode numbers in the same mode order is 0.249 nm by using Eq.12. The measured mode spacing of 0.25 nm, correlates well with the calculations.

The size parameter is estimated as $x \approx 2200$ at 1427.73 nm. The Si sphere can support up to $Nx \approx 7660$ mode number, since the polar angular mode number n of the WGMs around the microsphere are restricted by $x \leq n \leq Nx$, adequate for our case, as also recognized in Chapter 3.5.

The impact parameter for coupling to a microsphere is restricted by $a \leq b \leq ma$ [39]. Only the incident beams in this impact parameter region could couple to the microsphere. For our experiment, assuming the WG and the sphere are in contact, the impact parameter is $b \approx 520$ μm, satisfying the localization principle.

5.5 The Diamond Sphere

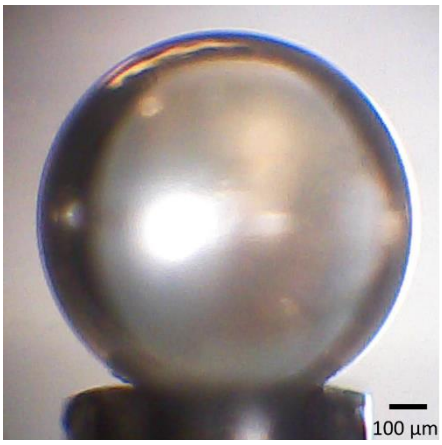

Figure 5.6: The image of the diamond sphere held by suction needle.

The 500 μm radius monocrystalline synthetic diamond microsphere is manufactured by Dutch Diamond Technologies using chemical vapor deposition (CVD) [53]. A specialized lapping machinery with a roundness form accuracy < 250 nm was used for reaching a spherical shape. Then, the spherical sample was polished finely for minimizing surface roughness, and acquire high

smoothness. To further increase the evanescent coupling, it is essential to have a smooth surface finish without any contaminants. The surface roughness is < 2 nm, and the diamond sphere is cleaned by an isopropanol and acetone mixture inside an ultrasonic bath to remove any surface contaminants. Our spherical diamond sample is classified as Type Ib, with a nitrogen impurity > 5 ppm, and has a refractive index of 2.38 in near-IR region wavelengths [54]. Figure 5.6 shows the image of the diamond sphere used for our purposes, taken with a visible camera. In Figure 5. 7, the optical visible camera image of the diamond sphere held by the suction needle can be seen at the front, and the diamond waveguide and the butt-coupled optical bare SM fiber can be seen at the back.

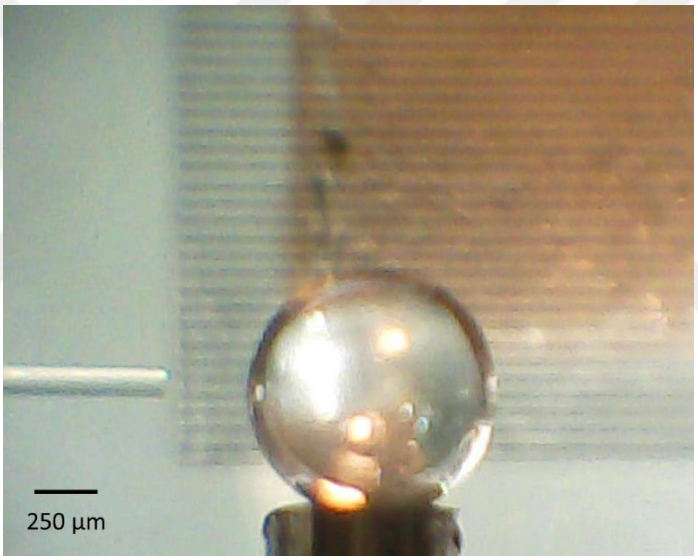

Figure 5. 7: The image of diamond sphere held by vacuumed needle tip placed on the diamond waveguide.

5.6 Experimental Results for Diamond Sphere

TE and TM polarized 90° elastic scattering (shown as the blue curves) and 0° transmission (shown as the red curves) spectra of the WGM resonances of the 1 mm-diamond sphere excited by a 20 µm deep shallow diamond waveguide for 1 nm wavelength sweep, from 1427.15 nm to 1428.15 nm are shown in the Figures 5.8 and 5.9, respectively.

The size parameter is estimated as $x \approx 2200$ at 1427.7 nm. The polar angular mode number n of the WGMs around the microsphere is restricted by $x \leq n \leq Nx$. Our diamond sphere can support mode number n from a minimum of 2200 up to $Nx \approx 5200$.

The impact parameter for coupling to a microsphere is restricted by $a \leq b \leq Na$ [39]. Only the incident beams in this impact parameter region could couple to the microsphere. For our experiment, assuming the WG and the sphere are in contact, the impact parameter is $b \approx 520$ µm, satisfying the localization principle with boundaries of 500 µm $\leq b \leq$ 1190 µm.

The polar angular mode number n, and radial mode order l define WGMs of a microsphere. WGMs of consecutive n and same radial mode order l form a mode family, and are separated by a mode spacing $\Delta\lambda = 0.341$ nm according to Eq. 12. The calculated mode spacing value correlates well with the value observed in the elastic scattering spectra of Figure 5.8 and 5.9.

The free spectral range (FSR) of Fabry - Pérot resonances of the diamond waveguide is calculated according to Eq. 5 as 0.086 nm. The FSR of the diamond WG Fabry - Pérot resonances, measured as 0.087 nm from the elastic scattering spectra of Figure 5.8 and 5.9, correlates well with the calculated value.

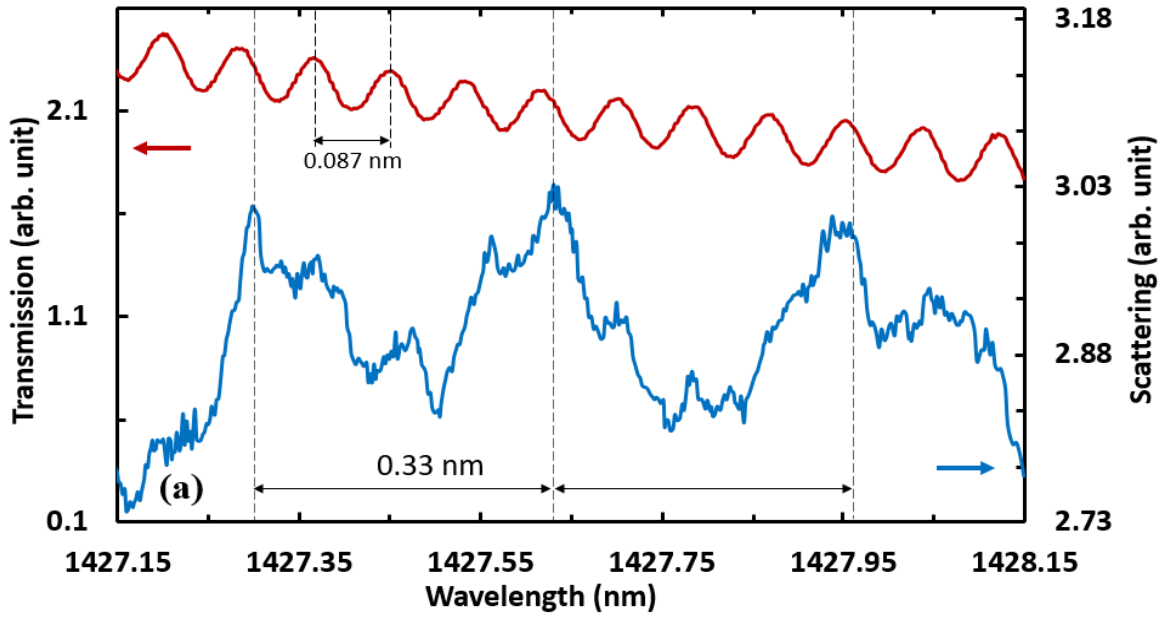

Figure 5.8: 0° transmission and TE polarized 90° elastic scattering from the diamond sphere on diamond WG.

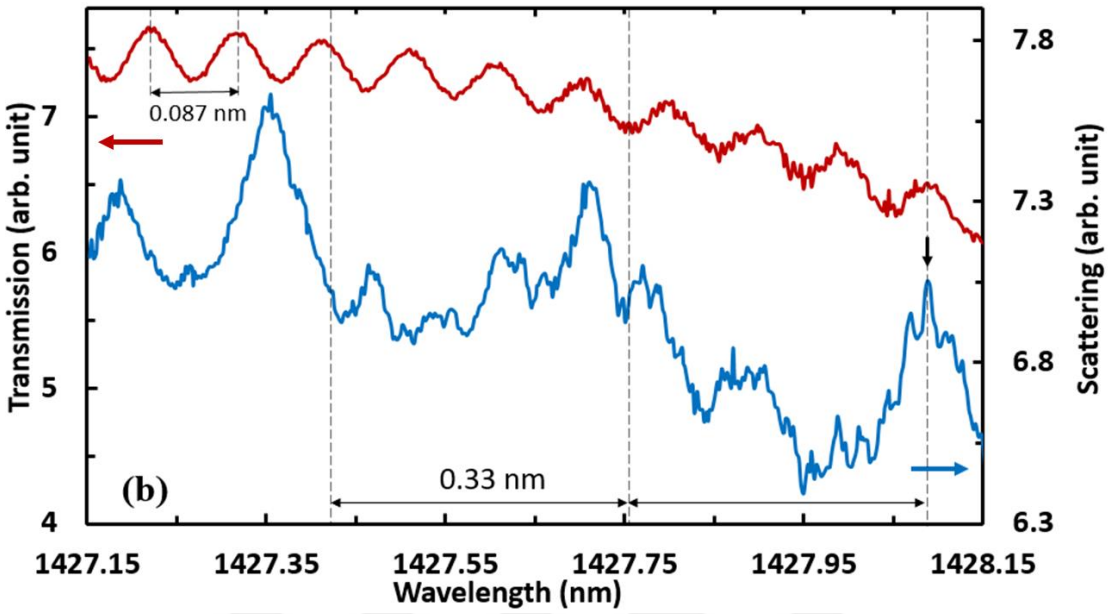

Figure 5.9: 0° transmission and TM polarized 90° elastic scattering from the diamond sphere on diamond WG.

Experimentally the Q-factor is determined using $Q = \lambda/\delta\lambda$, where λ is the resonance wavelength, and $\delta\lambda$ the full-width-at-half-maxima (FWHM) of the resonance. The narrowest high resolution peak is shown in Figure 5. 10, with $\delta\lambda$ = 9 pm FWHM, at a wavelength of 1428.09 nm. The Q-factor of this TM polarized peak is measured as 1.5 x 10^5. The measured Q-factor of the Fabry- Pérot resonances is on the order of 10^4, with a FWHM of 33 pm located around 1427.27 nm, during the 90° elastic scattering experiment.

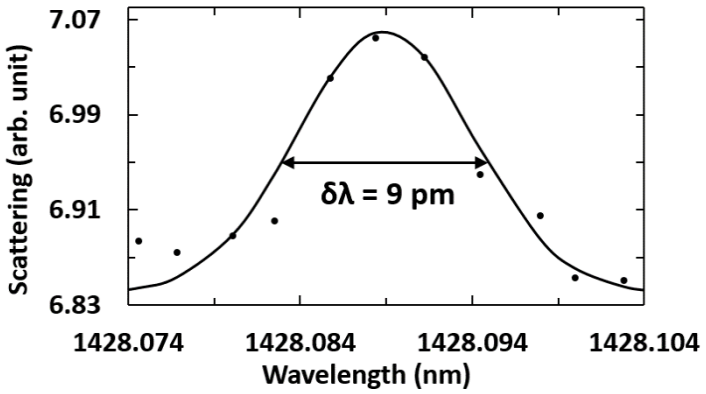

Figure 5. 10: TM polarized 90° WGM of the diamond sphere at 1428.088 nm with high-resolution.

Chapter 6

CONCLUSIONS

This work includes 1-mm silicon and diamond spheres' elastic light scattering observation using femtosecond (fs)-laser micromachined shallow Gorilla glass, Eagle$^{2000™}$ glass, and diamond waveguides produced at different writing speeds, depths, and laser powers.

In Chapter 1 the materials silicon, silica and diamond, microcavity, and waveguide structures, and coupling processes using these materials for observation of elastic scattering from spherical microcavities are briefly introduced.

Chapter 2 reviews the waveguide and the microsphere resonator properties, gives the fundamental background information for the designed experiments. Using the equations explained in Chapter 2, the expected results are calculated.

Elastic scattering of silicon sphere excited by fs-laser written Gorilla glass waveguides is presented in Chapter 3. The experimental setup, for observing the Gorilla glass waveguides end facets, and the light scattering of silicon sphere on a 25 μm deep fs-laser written Gorilla glass waveguide, is shown and explained in detail. For forming a clear mental image, visible camera images of the experimental setups are shared. Estimated experimental results and calculations for the light scattering of 1-mm silicon sphere excited by fs-laser written Gorilla glass waveguide are explained, compared, and concluded at the end of this chapter. Experimental results are also compared with the previous measurements with the same configurations [27] to ensure that, the system is working properly and also for observing the optical behavior of the 1-mm silicon sphere.

Chapter 4 shows the elastic scattering of silicon sphere excited by fs-laser written Eagle$^{2000™}$ glass waveguide. The waveguides are written to Eagle$^{2000™}$ glass with the same inscription method as Gorilla glass sample writing. Therefore, we urged to explore the elastic scattering results for 1-mm silicon sphere excited by Eagle$^{2000™}$ glass waveguide. Experimental setup for this configuration is explained in detail and the results are presented. The calculations and measurements are compared

and concluded. The results of this configuration and the previous chapter's configuration correlate well with each other.

Chapter 5 presents the two experimental configurations and their results by using fs-laser written Type-IIa (Nitrogen ~ 100 ppb) diamond waveguide as an excitation source. First, to testify that the fs-laser written diamond waveguide is functioning, elastic scattering of 1-mm silicon sphere is excited by the diamond waveguide. The results are compared and concluded with both estimated and calculated values, which agree well with each other. Thus, assuring the diamond waveguide sample can be used as an effective excitation source, as we already recognized the silicon sphere's consistency. At that point, we proceeded to demonstrate a novel all diamond system.

The all diamond system performs excitation of a Type Ib (Nitrogen > 5 ppm) 1-mm diamond sphere via a Type IIa fs-laser written shallow diamond waveguide. The diamond waveguide has a depth of 20 μm, and light propagates in a single mode with an elliptical mode shape. We observed high quality factor (on the orders of 10^5) whispering gallery modes, with a mode spacing of $\Delta\lambda$ = 0.33 nm, as well as Fabry-Pérot resonances triggered in the diamond waveguide, which have a free spectral range (FSR) of 87 pm, and relatively lower quality factors, as expected.

Spherical diamond microresonators on fs-laser written diamond WGs show promise as novel integrated photonic architectural components. Demonstration of such an integrated photonic platform may give rise to future nonlinear applications such as frequency comb generation, all diamond Raman amplifier, and high-power Raman laser [55] by utilizing NV centers or Raman scattering properties of diamond, as well as physical characteristics of diamond.

As future work, it may be possible to utilize in the current experimental setup, a single wavelength CW pump laser with high power to realize ultrahigh Q-factor, high power Raman lasing from the diamond microsphere by exploiting the high Raman gain and high-power handling capability of the diamond microsphere and the diamond waveguide.

VITA

Nurperi Yavuz completed her high school studies at Milli Eğitim Vakfı (MEV) Özel Ankara Fen Lisesi, Ankara, Turkey in 2010 as a merit scholarship student.

She received her Bachelor of Science (B.Sc.) degree in Physics from Middle East Technical University (METU) Ankara, Turkey in 2015. For her B. Sc. graduation thesis she worked on the characterization of nanocomposite samples by using Terahertz Time Domain Spectroscopy (THz-TDS) with Professor Hakan Altan of METU Department of Physics.

Later she enrolled at the Master of Science (M. Sc.) program in Optoelectronics and Photonics Engineering at Koç University in Istanbul, Turkey in 2016, as a teaching/research assistant. In 2017, she joined Koç University Microphotonics Research Laboratory, where she worked on "Elastic Light Scattering of Silicon and Diamond Microspheres Excited by Femtosecond Laser Written Glass and Diamond Waveguides" with Professor Ali Serpengüzel of Koç University Department of Physics towards the thesis requirement of her M. Sc. degree.

She intends to follow her academic work by applying it to integrated photonics industry, and pursue further academic endeavors in optics and photonics.

BIBLIOGRAPHY

[1] Lord Rayleigh, "CXII. The problem of the whispering gallery," London, Edinburgh, Dublin Philosophical Mag. J. Sci. **20**, 1001–1004 (1910).

[2] M. Noto, D. Keng, I. Teraoka, and S. Arnold, "Detection of protein orientation on the silica microsphere surface using transverse electric/transverse magnetic whispering gallery modes," Biophys. J. **92**, 4466–4472 (2007).

[3] A. Serpengüzel, Y. O. Yılmaz, U. K. Ayaz, and A. Kurt, "Silicon Microspheres for VLSI Photonics," in "*VLSI Micro- and Nanophotonics: Science, Technology, and Applications,"* E.-H. Lee, L. Eldada, M. Razeghi, and C. Jagadish, Eds. (CRC Press, Boca Raton, Florida 2011).

[4] V. S. Ilchenko, A. A. Savchenkov, A. B. Matsko, and L. Maleki, "Whispering-gallery-mode electro-optic modulator and photonic microwave receiver," J. Opt. Soc. Am. B **20**, 333–342 (2003).

[5] C. Wang, Y. Choi, J. Lee, E. Hu, J. Yang, and J. Butler, "Observation of whispering gallery modes in nanocrystalline diamond microdisks," Appl. Phys. Lett. **90**, 081110 (2007).

[6] H.-M. Tzeng, K. F. Wall, M. Long, and R. K. Chang, "Laser emission from individual droplets at wavelengths corresponding to morphology-dependent resonances," Opt. Lett. **9**, 499–501 (1984).

[7] L. Feng, Z. J. Wong, R.-M. Ma, Y. Wang, and X. Zhang, "Single-mode laser by parity-time symmetry breaking," Science **346**, 972–975 (2014).

[8] S. L. McCall, A. F. J. Levi, R. E. Slusher, S. J. Pearton, and R. A. Logan, "Whispering gallery mode microdisk lasers," Appl. Phys. Lett. **60**, 289–291 (1992).

[9] M. Cai, G. Hunziker, and K. Vahala, "Fiber-optic add-drop device based on a silica microsphere-whispering gallery mode system," IEEE Photon. Technol. Lett. **11**, 686–687 (1999).

[10] D. K. Armani, T. J. Kippenberg, S. M. Spillane, and K. J. Vahala, "Ultra-high-Q toroid microcavity on a chip," Nature **421**, 925–928 (2003).

[11] U. S. Gökay, M. Zakwan, A. Demir, and A. Serpengüzel, "Optical fiber excitation of Fano resonances in a silicon microsphere," Fiber Integrated Opt. **35**, 38–46 (2016).

[12] M. Cai, O. Painter, and K. J. Vahala, "Observation of critical coupling in a fiber taper to a silica-microsphere whispering-gallery mode system," Phys. Rev. Lett. **85**, 74–77 (2000).

[13] V. S. Ilchenko, A. M. Bennett, P. Santini, A. A. Savchenkov, A. B. Matsko, and L. Maleki, "Whispering gallery mode diamond resonator," Opt. Lett. **38**, 4320–4323 (2013).

[14] A. M. Prabhu, A. Tsay, Z. Han, and V. Van, "Ultracompact SOI microring add–drop filter with wide bandwidth and wide FSR," IEEE Photon. Technol. Lett. **21**, 651–653 (2009).

[15] T. Bilici, Ş. İşçi, A. Kurt, and A. Serpengüzel, "Microsphere-Based Channel Dropping Filter With an Integrated Photodetector," IEEE Photon. Technol. Lett. **16**, 476–478 (2004).

[16] V. Sandoghdar, F. Treussart, J. Hare, V. Lefèvre-Seguin, J.-M. Raimond, and S. Haroche, "Very low threshold whispering-gallery-mode microsphere laser," Phys. Rev. A **54**, R1777–R1780 (1996).

[17] F. Vollmer and S. Arnold, "Whispering-gallery-mode biosensing: label-free detection down to single molecules," Nature Methods **5**, 591–596 (2008).

[18] Y. O. Yılmaz, A. Demir, A. Kurt, and A. Serpengüzel, "Optical channel dropping with a silicon microsphere," IEEE Photon. Technol. Lett. **17**, 1662–1664 (2005).

[19] M. J. R. Heck, J. F. Bauters, M. L. Davenport, J. K. Doylend, S. Jain, G. Kurczveil, S. Srinivasan, Y. Tang, and J. E. Bowers, "Hybrid Silicon Photonic Integrated Circuit Technology," IEEE J. Selected Topics Quantum Electron. **19**, 6100117–6100117 (2013).

[20] W. Bogaerts, D. Taillaert, B. Luyssaert, P. Dumon, J. Van Campenhout, P. Bienstman, D. Van Thourhout, R. Baets, V. Wiaux, and S. Beckx, "Basic structures for photonic integrated circuits in Silicon-on-insulator," Opt. Express **12**, 1583-1591 (2004).

[21] I. Aharonovich, A. D. Greentree, and S. Prawer, "Diamond photonics," Nature Photon. **5**, 397 (2011).

[22] M. P. Hiscocks, K. Ganesan, B. C. Gibson, S. T. Huntington, F. Ladouceur, and S. Prawer, "Diamond waveguides fabricated by reactive ion etching," Opt. Express **16**, 19512-19519 (2008).

[23] R. S. Balmer, J. R. Brandon, S. L. Clewes, H. K. Dhillon, J. M. Dodson, I. Friel, P. N. Inglis, T. D. Madgwick, M. L. Markham, T. P. Mollart, N. Perkins, G. A. Scarsbrook, D. J. Twitchen, A. J. Whitehead, J. J. Wilman, and S. M. Woollard, "Chemical vapour deposition synthetic diamond: Materials, technology and applications," J. Phys. Condens. Mat. **21**, 364221 (2009).

[24] B. Jalali and S. Fathpour, "Silicon Photonics," J. Lightwave Technol. **24**, 4600-4615 (2006).

[25] V. B. Braginsky, M. L. Gorodetsky, and V. S. Ilchenko, "Quality-factor and nonlinear properties of optical whispering-gallery modes," Phys. Lett. A **137**, 393–397 (1989).

[26] A. Serpengüzel, S. Arnold, and G. Griffel, "Excitation of resonances of microspheres on an optical fiber," Opt. Lett. **20**, 654–656 (1995).

[27] H. O. Çirkinoğlu, M. M. Bayer, U. S. Gökay, A. Serpengüzel, B. Sotillo, V. Bharadwaj, R. Ramponi, and S. M. Eaton, "Silicon microsphere whispering gallery modes excited by femtosecond-laser-inscribed glass waveguides," Appl. Opt. **57**, 3687–3692 (2018).

[28] F. J. Himpsel, J. A. Knapp, J. A. van Vechten, and D. E. Eastman, "Quantum photoyield of diamond(111) - a stable negative-affinity emitter," Phys. Rev. B **20**, 624–627 (1979).

[29] H. Philipp and E. Taft, "Optical properties of diamond in the vacuum ultraviolet," Phys. Rev. **127**, 159 (1962).

[30] A. Chiasera, Y. Dumeige, P. Féron, M. Ferrari, Y. Jestin, G. Nunzi Conti, S. Pelli, S. Soria, and G. C. Righini, "Spherical whispering-gallery-mode microresonators," Laser Photon. Rev. **4**, 457–482 (2010).

[31] S. Prawer and I. Aharonovich, "*Quantum Information Processing with Diamond: Principles and Applications*" (Elsevier, Dordrecht, 2014).

[32] S. K. Selvaraja and P. Sethi, "Review on Optical Waveguides," in "*Emerging Waveguide Technology*," K. Y. You, Ed. (InTech Open, London, 2018).

[33] C. Fabry and A. Pérot, "Théorie et applications d'une nouvelle méthode de spectroscopie interférentielle," Ann. Chim. Phys. **16**, 115–144 (1899).

[34] K.Vahala, "*Optical Microcavities"* (World Scientific, Singapore, 2004).

[35] U. Keller, D. A. B. Miller, G. D. Boyd, T. H. Chiu, J. F. Ferguson, and M. T. Asom, "Solid-state low-loss intracavity saturable absorber for Nd:YLF lasers: an antiresonant semiconductor Fabry–Pérot saturable absorber," Opt. Lett. **17**, 505–507 (1992).

[36] N. Ismail, C. C. Kores, D. Geskus, and M. Pollnau, "Fabry-Pérot resonator: spectral line shapes, generic and related Airy distributions, linewidths, finesses, and performance at low or frequency-dependent reflectivity," Opt. Express **24**, 16366 (2016).

[37] C. F. Bohren and D. R. Huffman, "*Absorption and Scattering of Light by Small Particles"* (John Wiley and Sons, New York 2008) pp. 100.

[38] P. Chýlek, "Resonance structure of Mie scattering: distance between resonances," J. Opt. Soc. Am. A **7**, 1609–1613 (1990).

[39] A. Serpengüzel, S. Arnold, G. Griffel, and J. A. Lock, "Enhanced coupling to microsphere resonances with optical fibers," J. Opt. Soc. Am. B **14**, 790–795 (1997).

[40] M. L. Gorodetsky, A. A. Savchenkov, and V. S. Ilchenko, "Ultimate Q of optical microsphere resonators," Opt. Lett. **21,** 453-455 (1996).

[41] V. S. Ilchenko, M. L. Gorodetsky, and S. P. Vyatchanin, "Coupling and tunability of optical whispering-gallery modes: a basis for coordinate meter," Opt. Commun. **107**, 41-48 (1994).

[42] G. Griffel, S. Arnold, D. Taşkent, A. Serpengüzel, J. Connolly, and N. Morris, "Morphology-dependent resonances of a microsphere–optical fiber system," Opt. Lett. **21**, 695-697 (1996).

[43] N. Takeda, "Spherical silicon 1 mm device and its clustering," in "Proceedings of IEEE International Symposium on Advanced Packaging Materials: Processes, Properties, and Interfaces," (IEEE) 86–91 (2001).

[44] P. Chýlek, "Partial-wave resonances and the ripple structure in the Mie normalized extinction cross section," J. Opt. Soc. Am. **66**, 285-287 (1976).

[45] A. Ellison and I. A. Cornejo, "Glass Substrates for Liquid Crystal Displays," Int. J. Appl. Glass Sci. **1,** 87–103 (2010).

[46] "Eagle^{2000} Alkali free boro-aluminosilicate glass," Präzisions Glas & Optik GmbH, Iserlohn, 2018. Available online: https://www.pgo-online.com/intl/eagle2000.html.

[47] M. W. Doherty, N. B. Manson, P. Delaney, F. Jelezko, J. Wrachtrup, and L. C. L. Hollenberg, "The nitrogen-vacancy colour centre in diamond," Phys. Reports **528**, 1–45 (2013).

[48] Elisabeth Fraczek, Vasili G. Savitski, Matthew Dale, Ben G. Breeze, Phil Diggle, Matthew Markham, Andrew Bennett, Harpreet Dhillon, Mark E. Newton, and Alan J. Kemp, "Laser spectroscopy of NV^- and NV^0 colour centres in synthetic diamond," Opt. Mater. Express **7**, 2571-2585 (2017)

[49] A. D. Greentree, B. A. Fairchild, F. M. Hossain, and S. Prawer, "Diamond integrated quantum photonics," Materials Today **11**, 22–31 (2008).

[50] M. Ams, D. J. Little, and M. J. Withford, "Femtosecond-laser-induced refractive index modifications for photonic device processing," in "*Laser Growth and Processing of Photonic Devices*," N. A. Vainos, Ed. Woodhead, Elsevier, 2012, pp. 305–332.

[51] B. Sotillo, A. Chiappini, V. Bharadwaj, J. Hadden, F. Bosia, P. Olivero, M. Ferrari, R. Ramponi, P. Barclay, and S. Eaton, "Polarized micro-Raman studies of femtosecond laser written stress-induced optical waveguides in diamond," Appl. Phys. Lett. **112,** 031109 (2018).

[52] B. Sotillo, V. Bharadwaj, J. Hadden, M. Sakakura, A. Chiappini, T. T. Fernandez, S. Longhi, O. Jedrkiewicz, Y. Shimotsuma, and L. Criante, "Diamond photonics platform enabled by femtosecond laser writing," Nature Sci. Reports **6**, 35566 (2016).

[53] "Grades and Shapes," Dutch Diamond Technologies, Cuijk, 2018, available online: http://www.dd-technologies.com/grades-and-shapes/.

[54] H. Phillip and E. Taft, "Kramers-Kronig analysis of reflectance data for diamond," Phys. Rev. **136**, A1445 (1964).

[55] J.-P. M. Feve, K. E. Shortoff, M. J. Bohn, and J. K. Brasseur, "High average power diamond Raman laser," Opt. Express **19**, 913 (2011).